bioRxiv preprint doi: https://doi.org/10.1101/2021.04.01.438121; this version posted April 2, 2021. The copyright holder for this preprint (which was not certified by peer review) is the author/funder, who has granted bioRxiv a license to display the preprint in perpetuity. It is made available under aCC-BY 4.0 International license.

Physical constraints on growth dynamics guide *C. elegans* developmental trajectories and animal shape

Joy Nyaanga[1,2], Christina Goss[3], Gaotian Zhang[1], Hannah N. Ahmed[1], Elliot J. Andersen[1], Isabella R. Miller[1], Justine K. Rozenich[1], Iris L. Swarthout[1], Jordan A. Vaughn[1], Erik C. Andersen[1], Niall M. Mangan[3], and Sasha Shirman[3]

1. Department of Molecular Biosciences, Northwestern University, Evanston, IL 60208, USA
2. Interdisciplinary Biological Sciences Program, Northwestern University, Evanston, IL 60208, USA
3. Department of Engineering Sciences and Applied Mathematics, Northwestern University, Evanston, IL 60208, USA

Keywords: Developmental growth; growth control; *C. elegans*; feeding dynamics; growth dynamics; stretcher model

Acknowledgements: We thank Jiping Wang and Keren Li for helpful advice about statistical data-analysis. We would like to thank members of the Andersen laboratory and the Mangan group for their helpful comments on the manuscript.

Funding: For this work, J.N., C.G., G.Z., E.C.A., N.M.M, and S.S. received support from the NSF-Simons Center for Quantitative Biology at Northwestern University (awards Simons Foundation/SFARI 597491-RWC and the National Science Foundation 1764421). C.G., S.S., and N.M.M. received support from the National Science Foundation RTG: Interdisciplinary Training in Quantitative Biological Modeling, award 1547394). C.G. was supported in part by the Murphy Scholars Program of the Robert R. McCormick School of Engineering and Applied Science at Northwestern University.

bioRxiv preprint doi: https://doi.org/10.1101/2021.04.01.438121; this version posted April 2, 2021. The copyright holder for this preprint (which was not certified by peer review) is the author/funder, who has granted bioRxiv a license to display the preprint in perpetuity. It is made available under aCC-BY 4.0 International license.

Competing interests: The authors have no competing interests.

Emails and ORCIDs:

JN: JoyNyaanga2024@u.northwestern.edu, 0000-0002-1402-9213

CG: christinagoss2021@u.northwestern.edu, 0000-0002-5715-3337

GZ: gaotian.zhang@northwestern.edu, 0000-0001-6468-1341

HNA: hannahahmed02@gmail.com

EJA: elliotjandersen@gmail.com

IRM: miller.ir18@gmail.com

JKR: justine.rozenich@icloud.com

ILS: IrisSwarthout2023@u.northwestern.edu

JAV: JordanVaughn2023@u.northwestern.edu

ECA: erik.andersen@gmail.com, 0000-0003-0229-9651

NMM: niallmm@gmail.com, 0000-0002-3491-8341

SS: shirman.sasha@gmail.com, 0000-0001-5855-9470

bioRxiv preprint doi: https://doi.org/10.1101/2021.04.01.438121; this version posted April 2, 2021. The copyright holder for this preprint (which was not certified by peer review) is the author/funder, who has granted bioRxiv a license to display the preprint in perpetuity. It is made available under aCC-BY 4.0 International license.

Author contributions

Conceptualization: Joy Nyaanga, Gaotian Zhang, Christina Goss, Sasha Shirman, Niall M. Mangan, Erik C. Andersen

Formal analysis: Joy Nyaanga, Sasha Shirman

Funding acquisition: Erik C. Andersen, Niall M. Mangan

Investigation: Joy Nyaanga, Gaotian Zhang, Erik C. Andersen

Manual image processing: Joy Nyaanga, Hannah N. Ahmed, Elliot J. Andersen, Isabella R. Miller, Justine K. Rozenich, Iris L. Swarthout, Jordan A. Vaughn

Methodology: Joy Nyaanga, Gaotian Zhang, Christina Goss, Sasha Shirman

Project Administration: Erik C. Andersen, Niall M. Mangan

Resources: Erik C. Andersen

Supervision: Erik C. Andersen, Niall M. Mangan

Validation: Joy Nyaanga, Gaotian Zhang

Visualization: Joy Nyaanga, Sasha Shirman

Writing - original draft: Joy Nyaanga, Sasha Shirman, Christina Goss

Writing - review & editing: Joy Nyaanga, Sasha Shirman, Christina Goss, Gaotian Zhang, Erik C. Andersen, Niall M. Mangan

bioRxiv preprint doi: https://doi.org/10.1101/2021.04.01.438121; this version posted April 2, 2021. The copyright holder for this preprint (which was not certified by peer review) is the author/funder, who has granted bioRxiv a license to display the preprint in perpetuity. It is made available under aCC-BY 4.0 International license.

Abstract

Growth control is essential to establish organism size, so organisms must have mechanisms to both sense and adjust growth. Studies of single cells have revealed that size homeostasis can be achieved using distinct control methods: Sizer, Timer, and Adder. In multicellular organisms, mechanisms that regulate body size must not only control single cell growth but also integrate it across organs and tissues during development to generate adult size and shape. To investigate body size and growth control in metazoans, we can leverage the roundworm *Caenorhabditis elegans* as a scalable and tractable model. We collected precise growth measurements of thousands of individuals throughout larval development, measured feeding behavior to pinpoint larval transitions, and quantified highly accurate changes in animal size and shape during development. We find differences in the growth of animal length and width during larval transitions. Using a combination of quantitative measurements and mathematical modeling, we present two physical mechanisms by which *C. elegans* can control growth. First, constraints on cuticle stretch generate mechanical signals through which animals sense body size and initiate larval-stage transitions. Second, mechanical control of food intake drives growth rate within larval stages, but between stages, regulatory mechanisms influence growth. These results suggest how physical constraints control developmental timing and growth rate in *C. elegans*.

Author summary

Precise growth control is essential to the development of proper adult body size and shape. Although a larger body size can increase an organism's competitive advantage, an increased body size also requires added time and nutrients to develop. As such, organisms must have mechanisms to both sense and adjust growth during development. Studies of single cells have revealed that proper body size can be achieved using size or time control mechanisms. In multicellular organisms, additional levels of control are required as growth must be differentially regulated across cells, tissues, and organs. We leveraged the roundworm *Caenorhabditis elegans* as a scalable model to investigate growth control in metazoans. As animals transitioned from one developmental stage to the next, we observed changes in body shape while body size remained constant,

bioRxiv preprint doi: https://doi.org/10.1101/2021.04.01.438121; this version posted April 2, 2021. The copyright holder for this preprint (which was not certified by peer review) is the author/funder, who has granted bioRxiv a license to display the preprint in perpetuity. It is made available under aCC-BY 4.0 International license.

suggesting that animals might sense shape to set developmental timing. Two mechanisms likely control growth rate, physical control of feeding rate and metabolic regulation, and we are able to identify developmental periods where each govern growth. Our results demonstrate how physical constraints in tandem with other regulation can be used to broadly control developmental timing and growth rate across diverse organisms.

bioRxiv preprint doi: https://doi.org/10.1101/2021.04.01.438121; this version posted April 2, 2021. The copyright holder for this preprint (which was not certified by peer review) is the author/funder, who has granted bioRxiv a license to display the preprint in perpetuity. It is made available under aCC-BY 4.0 International license.

Introduction

Growth is a complex process fundamental to development. Individual cells and whole animals must reach an appropriate size to remain competitive in their environment. A larger body size conveys many selective advantages to an organism, including increased predation success or defense against predation, increased success in mating, and increased success in intraspecific as well as interspecific competition. Offsetting these advantages, larger organisms require more food resources to grow, take longer to develop, and produce fewer offspring [1]. Therefore, it is critical for multicellular organisms to effectively coordinate the growth of both individual cells and the whole body. Additionally, growth at both of these scales must be coupled with developmental progression to ensure the proper timing of irreversible developmental events.

In recent years, efforts have focused on understanding how organisms control growth to achieve size homeostasis [2–4]. Many of these studies are motivated by the decades-long debate about whether growth is linear or exponential; two separate models each having unique implications for size regulation. In a linear model with constant growth rate, smaller organisms must grow proportionally more than larger organisms to maintain size homeostasis. In this paradigm, organism size can be controlled simply by specifying growth duration. Subsequently, this method of growth control is named the ‘Timer’ model [5,6]. Instead of regulating growth duration, organisms can monitor size and adjust duration of growth to reach an optimal size, often named the ‘Sizer’ model [7–9]. In an exponential model, growth rate is proportional to size. Here, a time-based control mechanism alone would fail to maintain size homeostasis because larger organisms would grow proportionally more during a specified period of time. This difference in growth requires a size-based control mechanism to ensure that growth is halted once a maximum size is reached. Although ‘Timer’ and ‘Sizer’ are the most often proposed size-control models, other models have been suggested, including ‘Adder’ in which a fixed amount of material is added to a cell or organism during growth [10,11]. It is not trivial to determine which model most accurately describes growth of individual cells or whole organisms because quantitative measurements of growth must be collected at high precision and throughput under tightly controlled experimental conditions. In unicellular organisms, the development of high-throughput experimental techniques

bioRxiv preprint doi: https://doi.org/10.1101/2021.04.01.438121; this version posted April 2, 2021. The copyright holder for this preprint (which was not certified by peer review) is the author/funder, who has granted bioRxiv a license to display the preprint in perpetuity. It is made available under aCC-BY 4.0 International license.

in combination with theoretical models have advanced the understanding of size control [12–16]. Progress has been slower for multicellular organisms because cell growth within tissues and tissue growth within organisms often progress at different rates, suggesting that they are likely not regulated in the same ways [17–19].

The nematode *Caenorhabditis elegans* presents both a scalable and tractable multicellular animal model to study growth control. With an adult body length of approximately 1 mm, hundreds of thousands of individuals are easily cultured in controlled laboratory conditions [20]. Moreover, *C. elegans* post-embryonic development is marked by several molts that provide clear developmental milestones [21]. Each molt is initiated by a period of inactivity (lethargus) and terminated once the animal successfully sheds its collagen-rich outer cuticle (ecdysis) [22]. Four molts separate the *C. elegans* life cycle into five distinct stages: four larval stages (L1-L4) and adult. The timing of these molts determines the completion of stage-specific development [23,24] and underscores the importance of growth regulation during *C. elegans* larval development.

A full description of an organism's development includes the assessment of how growth and body size are regulated. Initial studies of *C. elegans* development described whole-organism growth as a sigmoidal curve characterized by continuous larval growth in length that reaches saturation in adulthood [25]. These early studies hypothesized that molt events had little effect on continuous growth as the *C. elegans* cuticle allowed for stretch during larval stages. Later work determined that larval progression was not continuous but rather piecewise in nature [26]. This study showed that *C. elegans* volumetric growth rate increased from stage to stage such that L1 animals had the slowest rate of growth and L4 animals had the fastest. This finding suggests that *C. elegans* have a mechanism for regulating growth rate, potentially at each molt. Most recently, researchers using single-animal imaging strategies observed that animals did not advance to the next developmental stage until a critical volume was reached [27]. This finding suggests that *C. elegans* growth follows a 'Sizer' model with each molt decision controlled by a volume threshold and further implies that animals are able to communicate information about body size to precisely regulate growth.

bioRxiv preprint doi: https://doi.org/10.1101/2021.04.01.438121; this version posted April 2, 2021. The copyright holder for this preprint (which was not certified by peer review) is the author/funder, who has granted bioRxiv a license to display the preprint in perpetuity. It is made available under aCC-BY 4.0 International license.

Extensive characterization of *C. elegans* body size mutants has revealed several processes that influence growth rate and body size [28]. A number of genes act through signaling pathways to influence growth and body size [29,30]. Some of these pathways contribute to body size control by regulating cuticle collagen genes [31]. Alternatively, mutations in some cuticle collagen genes directly disrupt the physical structure of the cuticle [32]. These structural changes act as physical constraints on growth as opposed to regulatory mechanisms of growth control. Environment factors also play a significant role in *C. elegans* growth control. Food restriction is known to decrease growth rate or, when extreme, induce complete developmental arrest [27,33,34]. In *C. elegans*, mutations that disrupt the ability to properly consume food also cause individuals to be small and thin, indicating that food intake can act as a physical constraint on growth and body shape [35].

To understand *C. elegans* growth control at the whole-organism level, precise measurements of body size and shape for large numbers of individuals are required. Using a combination of quantitative growth measurements and mathematical modeling, we performed a high-resolution longitudinal study of *C. elegans* larval progression and captured high-precision details about animal length, width, volume, and feeding dynamics. By investigating *C. elegans* feeding and growth in tandem for thousands of individual animals, we found decreases in feeding behavior associated with each larval transition that were also correlated in time with changes in growth. We used our large-scale measurements of body size to further analyze the periods of time surrounding each larval transition. At each molt, we observed simultaneous increases in length, decreases in width, and maintenance of volume, suggesting that body shape in addition to size plays a role in the control of *C. elegans* growth. Given these data, we propose a “Stretcher” mechanism for growth control whereby *C. elegans* senses body size through physical constraints on cuticle stretch and undergoes larval-stage transitions when the cuticle reaches its maximum capacity for stretch. Additionally, we propose that *C. elegans* are able to physically constrain growth rate by the mechanical control of food intake. We used quantitative models of eating and growth to evaluate our data and predicted that the rate of volumetric growth is primarily controlled by animal feeding rate for most of development. However, at critical time points, including larval transitions, volumetric

bioRxiv preprint doi: https://doi.org/10.1101/2021.04.01.438121; this version posted April 2, 2021. The copyright holder for this preprint (which was not certified by peer review) is the author/funder, who has granted bioRxiv a license to display the preprint in perpetuity. It is made available under aCC-BY 4.0 International license.

166 growth rate was no longer primarily controlled by food intake and therefore other processes must control
167 resource allocation to influence growth.
168

169 Methods

170 Worm culture

171 The canonical laboratory strain N2 was obtained from the *C. elegans* Natural Diversity Resource [36]. Animals
172 were cultured at 20°C on 6 cm plates of modified nematode growth media (NGMA), which contained 1% agar
173 and 0.7% agarose seeded with *E. coli* OP50 bacteria [37].
174

175 Bacterial food

176 *E. coli* HB101 bacteria were prepared from cultures grown for 15 hours in Superbroth and then pelleted by
177 centrifugation. HB101 bacteria were diluted to OD100 in K medium (51 mM NaCl, 32 mM KCl, 3 mM CaCl2,
178 and 3 mM MgSO4 in distilled water) and stored at -80°C. Bacteria were thawed and fed to animals at a
179 concentration sufficient to sustain population growth from hatching to adulthood (OD20).
180

181 Growth of the animals

182 Populations of animals were propagated on NGMA plates for two generations without starvation. In the third
183 generation, gravid adults were bleach-synchronized [38]. Embryos were resuspended in K medium, aliquoted
184 into a 500 mL flask at a concentration of one embryo per µL, and allowed to hatch overnight. The following day,
185 arrested L1s were fed HB101 bacteria at a final concentration of OD20 in a final flask volume of 100 mL K
186 medium and HB101 food. Animals were grown for three days at 20°C with constant shaking. Following these
187 three days, adult animals were bleach-synchronized once more and embryos were aliquoted to seven replicate
188 500 mL flasks at a concentration of one embryo per µL in 100 mL. The following morning, six flasks were fed
189 HB101 bacterial food at a final concentration of OD20 in a final flask volume of 100 mL K medium and HB101
190 food. Two additional flasks were included to control for L1 animal size and possible clumping of bacterial food:
191 one flask contained L1 larvae but did not have food added and one flask contained no larvae but the same

bioRxiv preprint doi: https://doi.org/10.1101/2021.04.01.438121; this version posted April 2, 2021. The copyright holder for this preprint (which was not certified by peer review) is the author/funder, who has granted bioRxiv a license to display the preprint in perpetuity. It is made available under aCC-BY 4.0 International license.

concentration of HB101 bacteria as the six flasks containing L1 larvae. All replicate flasks were kept in an incubator at 20°C with shaking for the duration of the experiment. A small temperature gradient of 1.25°C was recorded in the shaking incubator with the highest temperature readings on the right side and lowest temperature readings on the left side (S1 File). This slight variation in temperature contributed to variation in developmental rate among replicates based on position within the incubator (replicates were placed in numerical order with replicate 1 positioned on the far right side of the incubator).

High-throughput measurements of body size and fluorescence

Flasks were sampled each hour beginning one hour after feeding and continuing for 72 consecutive hours. At each hour, 500 µL was removed from each flask and transferred to a well of a deep 96-well plate. Each flask was sampled at each time point. Fluorescent polychromatic beads (Polysciences, 19507-5) with a 0.5 µm particle size were added to each well at a final concentration of $3.64x10^8$ beads/mL and incubated at 20°C for 10 minutes with shaking. Following the bead incubation, 30 µL from each well of the deep 96-well plate was aliquoted to a 96-well microtiter plate. The process was repeated 11 times to 11 separate wells of the same microtiter plate with pipetting to mix the well contents from the deep 96-well plate. Animals were then treated with sodium azide at a final concentration of 50 mM to paralyze and prevent defecation of the ingested beads. The 96-well plate was imaged with an ImageXpress Nano (Molecular Devices, SanJose, CA) at both 2x and 10x magnification. The ImageXpress Nano acquires brightfield images using a 4.7 megaPixel CMOS camera. Images are stored in 16-bit TIFF format. Finally, animals were scored using a large-particle flow cytometer (COPAS BIOSORT, Union Biometrica, Holliston MA). The COPAS BIOSORT sheath flow rate was kept at a constant 10.3 ±0.1 mL per minute to reduce variability in length measurements.

Image processing

Manual measurements of animal size were performed using the free Java image-processing program ImageJ [39]. Well images for the six replicate flasks, excluding controls were loaded into ImageJ software. Length was measured from head to tail, and width was measured at the widest point of the animal. Five animals were

bioRxiv preprint doi: https://doi.org/10.1101/2021.04.01.438121; this version posted April 2, 2021. The copyright holder for this preprint (which was not certified by peer review) is the author/funder, who has granted bioRxiv a license to display the preprint in perpetuity. It is made available under aCC-BY 4.0 International license.

measured per well across thirty total wells for each hour. Measurements were repeated for all 72 time points in the assay. Body length and width were used to estimate animal area and volume by approximating the animal as a cylinder. Pixels were converted to µm using a conversion factor of 3.2937 pixels/µm.

Data processing

The COPAS BIOSORT was used to collect measurements of animal length (TOF), optical extinction (EXT), and fluorescence for every animal in each well. These traits measure properties of nematode development and, as such, increase as animals progress to adulthood [40]. Optical extinction measurements are the amount of light absorbed over the full length of an animal as it passes through the instrument. An additional measurement (norm.EXT) can be calculated by normalizing optical extinction by length. The raw data collected were imported and processed using the *easysorter* R package [41].

The COPAS BIOSORT data were analyzed further using Gaussian finite mixture modeling as implemented in the *mclust* R package [42]. These probabilistic models assume that data are generated from a mixture of multivariate normal distributions and, therefore, can be used to classify unstructured data into meaningful groups. Specifically, the *mclust* package fits a mixture model to data and selects the optimal number of clusters using an expectation-maximization algorithm and Bayes Information Criteria. For model-based clustering, log transformed animal length (logTOF) and log transformed optical extinction (logEXT) were used as inputs for the *Mclust* function. Data from each hour of the experiment was analyzed by replicate and clusters that did not appear to include majority animal objects were identified and removed as described previously [43]. This processing removed non-animal objects such as bacterial clumps, shed cuticles, and next generation larval animals from the time-course data.

We used a numpy polyfit regression of well-median data from the COPAS BIOSORT and image measurements to convert TOF and norm.EXT data to microns (S5 File, Eq. S7-S9). Only the unit-corrected BIOSORT data were used for further analysis.

bioRxiv preprint doi: https://doi.org/10.1101/2021.04.01.438121; this version posted April 2, 2021. The copyright holder for this preprint (which was not certified by peer review) is the author/funder, who has granted bioRxiv a license to display the preprint in perpetuity. It is made available under aCC-BY 4.0 International license.

Molt analysis

Fluorescence data obtained from the COPAS BIOSORT was used as a proxy for feeding behavior to distinguish animals in a molt from growing animals. First, fluorescence was normalized by EXT to account for the ability of larger animals to consume more food and beads. Next, an analysis of variance statistical model was fit to the fluorescence data normalized by EXT to determine the amount of variance contributed by replicate and well (Table S1). A local kernel regression smoothing method was then applied to the residuals of the variance analysis using the *lokern* R package [44]. Residuals were used to address only the differences over time and ignore minor variation among replicates and wells. The local minima of the regression function were found by solving for where the first derivative of this function equaled zero. The time associated with each local minimum was used to represent the timing of each molt. Molts occurred at 14, 25, 36, and 48 hours.

To identify periods of time that contained a majority of growing animals, the inflection points of the regression function were calculated by solving for where the second derivative of the function equaled zero. Time points between inflection points that did not contain a local fluorescence minimum were considered as growth periods. These hours were 1-13, 17-22, 27-32, and 39-45 corresponding to L1, L2, L3, and L4 growth periods.

Each molt is initiated when animals enter lethargus: a behavioral state where animals cease active feeding. To classify individual animals as in a molt or growing, we set a quiescence threshold using fluorescence measurements at each local minimum. The fluorescence measurement at each local minimum was as follows: 0.07, 0.06, 0.06, 0.06. The average of these measurements (0.06) was used as the fluorescence threshold signifying quiescent behavior. Any individual animals that fell below this threshold fluorescence value were designated as in a molt and animals above this threshold value were classified as growing.

bioRxiv preprint doi: https://doi.org/10.1101/2021.04.01.438121; this version posted April 2, 2021. The copyright holder for this preprint (which was not certified by peer review) is the author/funder, who has granted bioRxiv a license to display the preprint in perpetuity. It is made available under aCC-BY 4.0 International license.

Comparison of model fits

To determine the volume growth model, we fit linear, exponential, and cubic functions to data designated as growth periods for each larval stage. Both linear and nonlinear functions were fitted using least-squares regression. Akaike's information criterion (AIC) [45] and Bayesian information criterion (BIC) [46] were goodness of fit criteria used to evaluate candidate models. To assess the strength of evidence for each candidate model, we identified the model with the smallest AIC/BIC value and assessed the difference between this value and the AIC/BIC of the other two models. The magnitude of the difference was used to determine the level of support for each candidate model as previously described [47,48]. All model fits and analysis were performed using the *stats* R package.

Stretcher and feeding model analysis

To analyze shape dynamics, length and width data from growth time periods were extracted from the full COPAS BIOSORT population data and analyzed from each replicate separately to avoid issues with replicate variability. For replicate 2, the hours defining growth periods were 1-13, 16.37-22.39, and 26.93-32.96; corresponding to L1, L2, and L3. Hours defining larval stages were rounded as data was collected at exact hour increments. The L4 stage was excluded from the analysis because of the high variability within the population. We applied a local kernel regression, *lokern* R package [49], to smooth the population dynamics of length and width. To calculate mean and standard deviation, the smoothed population measurements were bootstrapped using 2,000 samples with replacement (S5 File, Algorithm S1). To determine cuticle properties throughout larval stages, we calculated the mean ratio of derivatives of regression width and length. Error for this ratio was calculated using error propagation to pass the bootstrap variation through the ratio (S5 File, Eq. S24-28).

To analyze volumetric growth dynamics and feeding dynamics, volume regression was calculated using a cylindrical approximation for animal shape (S5 File, Eq. S7-S9) and the same local kernel regression previously described was applied to red fluorescence data. Volume growth rate was calculated using the

bioRxiv preprint doi: https://doi.org/10.1101/2021.04.01.438121; this version posted April 2, 2021. The copyright holder for this preprint (which was not certified by peer review) is the author/funder, who has granted bioRxiv a license to display the preprint in perpetuity. It is made available under aCC-BY 4.0 International license.

python numpy gradient function applied to the volume regressions. An additional moving time window average (1.4 hours) was applied to smooth numerical errors in the derivative when determining feeding and growth regime transition points (S13 Fig).

Data availability

The authors state that all data necessary to confirm the conclusions of this work are within the text, figures, and supporting information files. All files and code for analysis and generation of figures and tables present within the article are archived on GitHub (https://github.com/AndersenLab/C.elegans-growth-manuscript).

Results

Quantitative measurements of *C. elegans* growth

We have optimized a quantitative growth assay that reliably measures small changes in *C. elegans* body size throughout development (Fig 1). Our method provides both high-throughput and high-precision assessment of developmental growth. In brief, populations of 100,000 animals were cultured in flasks. Every hour after feeding, a sample of the population from each flask (~300 animals/flask) was collected to measure animal length, width, and feeding rate. The ImageExpress imaging system was used to collect images of sampled animals. Feeding rate, examined using fluorescent microspheres, and body size were then measured using the COPAS BIOSORT. The imaging platform allowed for the further analysis of life stage and body size, contributing added precision to our measurements. We cultured six replicate populations of *C. elegans* for a total of 600,000 synchronized and growing animals. We sampled approximately 2,000 individuals each hour, generating highly scaled data to further assess *C. elegans* growth dynamics.

bioRxiv preprint doi: https://doi.org/10.1101/2021.04.01.438121; this version posted April 2, 2021. The copyright holder for this preprint (which was not certified by peer review) is the author/funder, who has granted bioRxiv a license to display the preprint in perpetuity. It is made available under aCC-BY 4.0 International license.

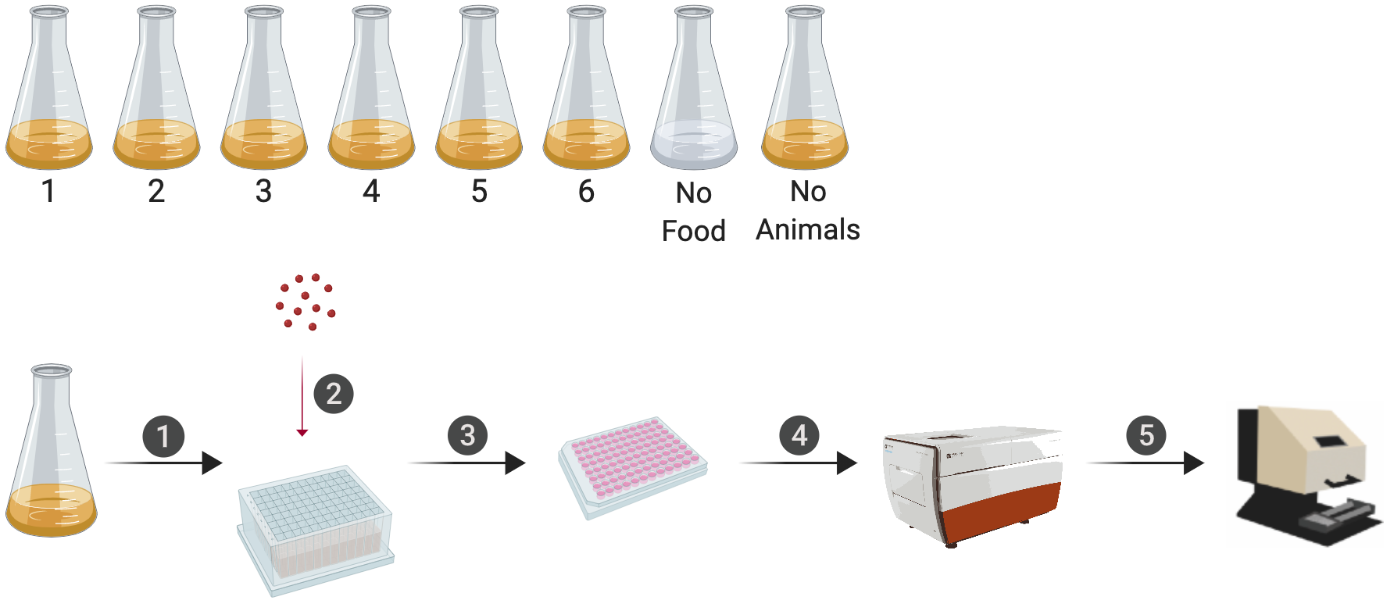

Fig 1. An overview of the quantitative growth assay.

Schematic of the experimental workflow is shown. Synchronized animals were cultured in flasks where six flasks contained replicate populations of nematodes, one flask had a population of unfed animals, and one flask only contained bacterial food. At each hour of the experiment, all eight flasks were sampled. In step 1, animals were transferred from each flask to a single well of a 96-well microtiter plate. In step 2, fluorescent beads were added to each well. Following a 10-minute incubation period, animals from each well of the deep-well plate were transferred to several wells of a 96-well microtiter plate for step 3. In step 4, animals in each well of the microtiter plate were imaged. In step 5, the same animals were measured using the COPAS BIOSORT. This process was repeated every hour after feeding for 72 consecutive hours (see Methods).

The raw data from the quantitative growth assay provides measurements of body size and feeding behavior, which are traits related to animal growth. Two measurements of body size were collected from raw data taken from the COPAS BIOSORT: time of flight (TOF) and optical extinction (EXT) (S1 Fig). Time of flight is a measurement of body length, and optical extinction is influenced by body length, thickness, and composition [40]. We investigated whether optical extinction could be correlated to a different measure of body size, through the collection of manual size measurements from images (see Methods). We calculated the median length, width, area, and volume of animals in a subset of imaged wells from each hour of the experiment. We

bioRxiv preprint doi: https://doi.org/10.1101/2021.04.01.438121; this version posted April 2, 2021. The copyright holder for this preprint (which was not certified by peer review) is the author/funder, who has granted bioRxiv a license to display the preprint in perpetuity. It is made available under aCC-BY 4.0 International license.

then compared these values to well median statistics from the processed COPAS BIOSORT data. We found a strong correlation between manual measurements of animal length from the image analysis and TOF measurements from the COPAS BIOSORT. We also observed an equally strong correlation between manual measurements of animal area and EXT as well as animal width and EXT normalized by body length (norm.EXT) (S2 Fig). We then approximated animal volume using measurements from the COPAS BIOSORT by using a cylindrical approximation for *C. elegans* shape (see Methods). This result expanded the number of body size parameters that we were able to assess using the COPAS BIOSORT data, allowing us to investigate growth dynamics in length, width, and volume (Fig 2A-C). To disentangle nematode objects from non-animal objects (bacteria clumps, detritus, shed cuticles), we employed model-based clustering to remove unwanted objects from analysis and better examine growth of animals (S3 Fig). Lastly, we converted COPAS BIOSORT measurements into microns (see Methods).

bioRxiv preprint doi: https://doi.org/10.1101/2021.04.01.438121; this version posted April 2, 2021. The copyright holder for this preprint (which was not certified by peer review) is the author/funder, who has granted bioRxiv a license to display the preprint in perpetuity. It is made available under aCC-BY 4.0 International license.

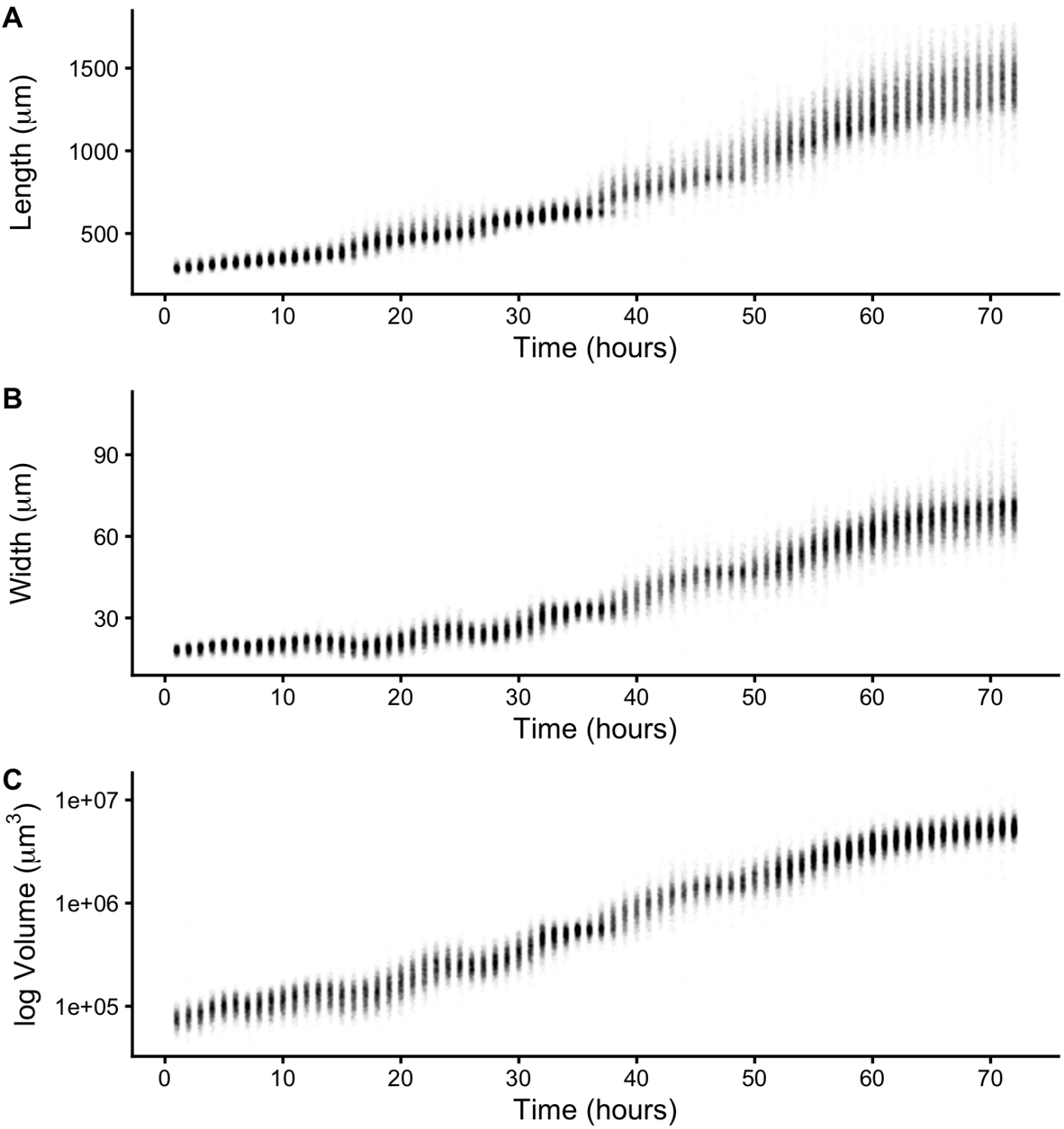

Fig 2. Quantitative measurements of animal size.

COPAS BIOSORT data of animal length (A), width (B), and volume (C) after the removal of non-animal objects using model-based clustering methods (see Methods).

bioRxiv preprint doi: https://doi.org/10.1101/2021.04.01.438121; this version posted April 2, 2021. The copyright holder for this preprint (which was not certified by peer review) is the author/funder, who has granted bioRxiv a license to display the preprint in perpetuity. It is made available under aCC-BY 4.0 International license.

We report body length, width, and volume of animals at each hour of development from L1 to adult (S1 Fig and Fig 2). Historically, growth of *C. elegans* has been shown as a sigmoidal curve where exponential growth during larval stages reaches a maximum rate in adulthood [25]. More recently, researchers have identified that growth curves are discontinuous during development punctuated by larval transitions [26,27]. Using our quantitative growth assay, we captured these small-scale discontinuities in larval growth as well as an apparent growth maximum during early adulthood. We noticed that all size variables (length, width, and volume) displayed these dynamics. Objects identified as animals appear to grow in size. However, in particular time windows during development, growth dynamics visibly shift, producing discontinuities in animal size. With these data, we were able to further investigate *C. elegans* growth and size control.

Fluorescence provides a quantitative measurement of animal feeding behavior and developmental progression

In addition to body size and shape, the raw data from the quantitative growth assay described above measured fluorescence of each animal object. To readily assess the thousands of measurements acquired at each hour, we generated summary statistics of median well measurements (S1 Table). With these summarized data, we investigated the relationship between feeding behavior and developmental stage. It is well established that temporary suspensions of *C. elegans* feeding occur during each molt [25,50]. As such, active feeding is frequently used to distinguish growing animals from individuals in a molt. We quantified feeding behavior by exposing animals to fluorescent beads the approximate size of bacteria and measuring fluorescence of animals [51]. Because larger animals are able to consume more food and therefore contain more ingested food, we normalized fluorescence by animal area to account for increases in body size (S4 Fig). The resulting fluorescence data showed a dynamic pattern (Fig 3A). At approximately 15 hours, fluorescence steadily increased to a peak before decreasing back to initial levels at approximately hour 27. This pattern, repeated three additional times, established clear time windows of local minimal fluorescence. These local minima represent periods of time where a large proportion of the population had reduced or ceased feeding and therefore suggests time windows where a majority of animals were likely not feeding because they were in a

bioRxiv preprint doi: https://doi.org/10.1101/2021.04.01.438121; this version posted April 2, 2021. The copyright holder for this preprint (which was not certified by peer review) is the author/funder, who has granted bioRxiv a license to display the preprint in perpetuity. It is made available under aCC-BY 4.0 International license.

molt. We used a local kernel regression method to estimate a smooth curve and calculate the derivative to identify the time associated with each local minimum (see Methods). We then assessed images collected from the growth assay and demonstrated that periods of decreased feeding are concurrent with the presence of shed cuticles, supporting that animals are undergoing a molt during these periods of time (S5 Fig). When we overlaid the timing of each local minimum on the population size data, we were able to outline the start and end of each larval stage (Fig 3B-D). Notably, local minima occur approximately every ten hours, consistent with well established observations of molt timing [25]. Furthermore, we observed a clear relationship between changes in feeding behavior and growth dynamics where decreases in feeding occurred simultaneously with discontinuous growth in length, width, and volume.

bioRxiv preprint doi: https://doi.org/10.1101/2021.04.01.438121; this version posted April 2, 2021. The copyright holder for this preprint (which was not certified by peer review) is the author/funder, who has granted bioRxiv a license to display the preprint in perpetuity. It is made available under aCC-BY 4.0 International license.

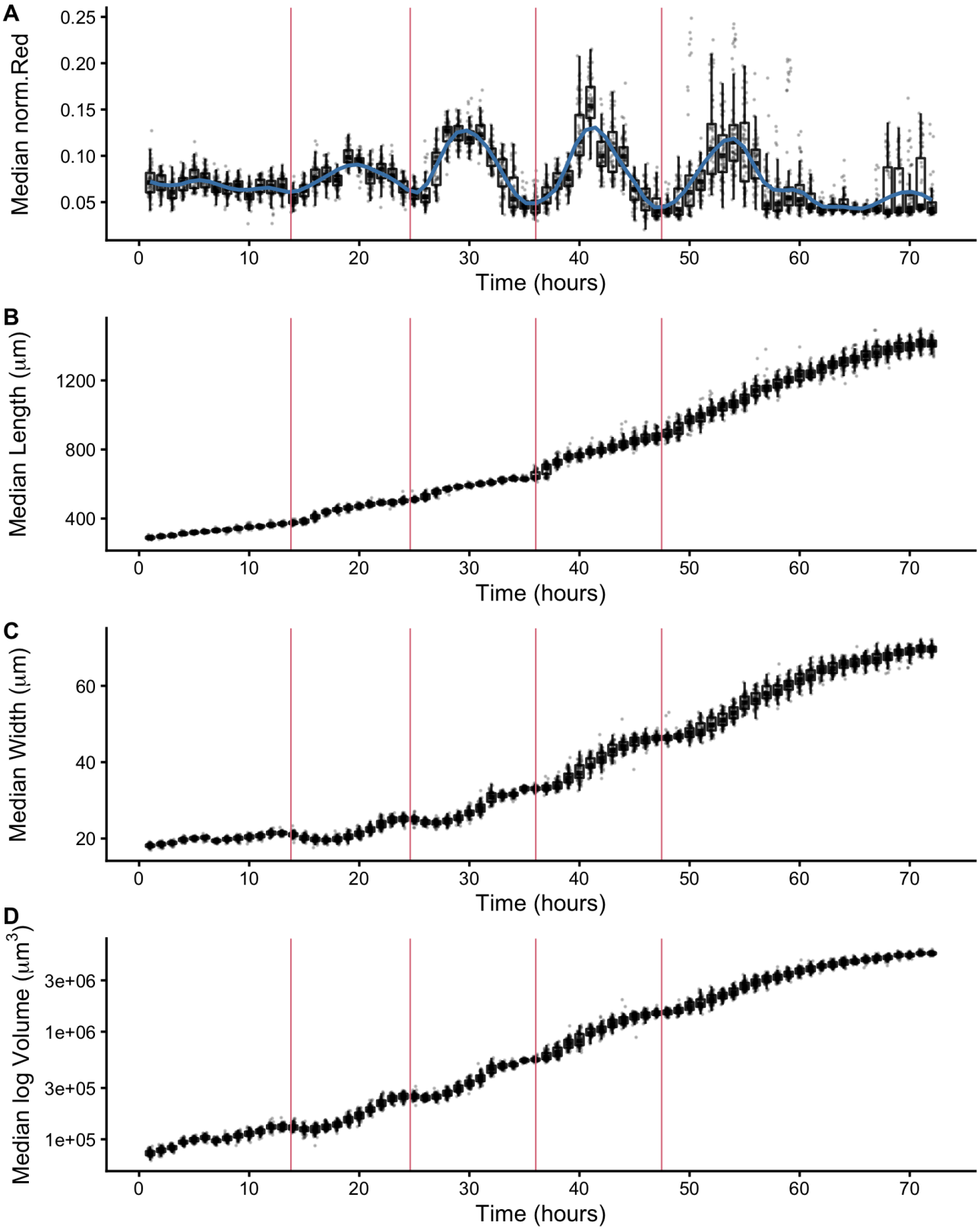

Fig 3. Fluorescence dynamics outline larval stages.

bioRxiv preprint doi: https://doi.org/10.1101/2021.04.01.438121; this version posted April 2, 2021. The copyright holder for this preprint (which was not certified by peer review) is the author/funder, who has granted bioRxiv a license to display the preprint in perpetuity. It is made available under aCC-BY 4.0 International license.

(A) Median normalized red fluorescence (y-axis) over time (x-axis) is shown. The blue line represents the kernel regression fit to the data. The red vertical lines correspond to the local minima of the regression and represent the transition between larval stages. Median length (B), median width (C), and median log volume (D) are shown with larval-stage transitions as well.

Changes in *C. elegans* body shape occur at larval-stage transitions

Adult body size is ultimately determined by the coordination of developmental progression and rate of growth. To understand how *C. elegans* achieve final size, we must first examine how *C. elegans* grow. Quantitative studies of *C. elegans* growth frequently assess changes in length or volume over time; however, to fully characterize changes associated with growth, it is also important to consider the dynamics of width. Two general models were proposed for *C. elegans* growth in volume: linear and exponential [25–27]. It is important to note that these volume growth models require different dynamics in length and width. To achieve linear volume growth, length and width must increase at precise sublinear rates that together result in a linear increase in volume. If animal length and width increased at a constant linear rate, then volume would increase at a cubic rate. Alternatively, if both length and width grew exponentially, then volume would fit an exponential model. We sought to identify which model best described *C. elegans* growth behavior but were unable to consistently distinguish between linear, exponential, and cubic models using statistical information criterion because of the similarity in the shapes of the growth curves (S6 Fig and S2 Table). This result is not surprising because computational simulations have shown that increases in experimental noise, above 2% added noise, limit the correct identification of growth models [52].

Growth has important implications for how animals regulate size. Size homeostasis requires that growth rate and developmental rate are coordinated. *C. elegans* reach a similar volume at each larval transition despite significant variation in individual growth rates [27]. Because individuals in a population maintain similar sizes despite differences in growth rate, a control mechanism to regulate developmental progression must exist.

bioRxiv preprint doi: https://doi.org/10.1101/2021.04.01.438121; this version posted April 2, 2021. The copyright holder for this preprint (which was not certified by peer review) is the author/funder, who has granted bioRxiv a license to display the preprint in perpetuity. It is made available under aCC-BY 4.0 International license.

Previous studies proposed a size-based growth control model in *C. elegans* where animals must reach a threshold size before advancing to the next developmental stage [27]. To assess changes in body size and shape during a larval transition, we examined the dynamics of animal length, width, and volume in the hours before, during, and after each molt. We find that for each shape variable, larger animals enter molt first (Fig 4). We also observe differences in the distributions of lengths during a larval transition compared to widths and volumes. Measurements of animal width and volume remain unimodal throughout a molt, but length does not. As larger animals begin to exit the molt, an increase in body length occurs that leads to the appearance of bimodality of lengths across the population. This length increase occurs simultaneously with a decrease in widths across the population. Importantly, volume remains constant while length increases and width decreases, indicating a change in body geometry not size (Fig 3 and Fig 4). These changes in the physical dimensions at each larval transition suggests that body shape, in addition to size, is involved in the control of *C. elegans* growth.

bioRxiv preprint doi: https://doi.org/10.1101/2021.04.01.438121; this version posted April 2, 2021. The copyright holder for this preprint (which was not certified by peer review) is the author/funder, who has granted bioRxiv a license to display the preprint in perpetuity. It is made available under aCC-BY 4.0 International license.

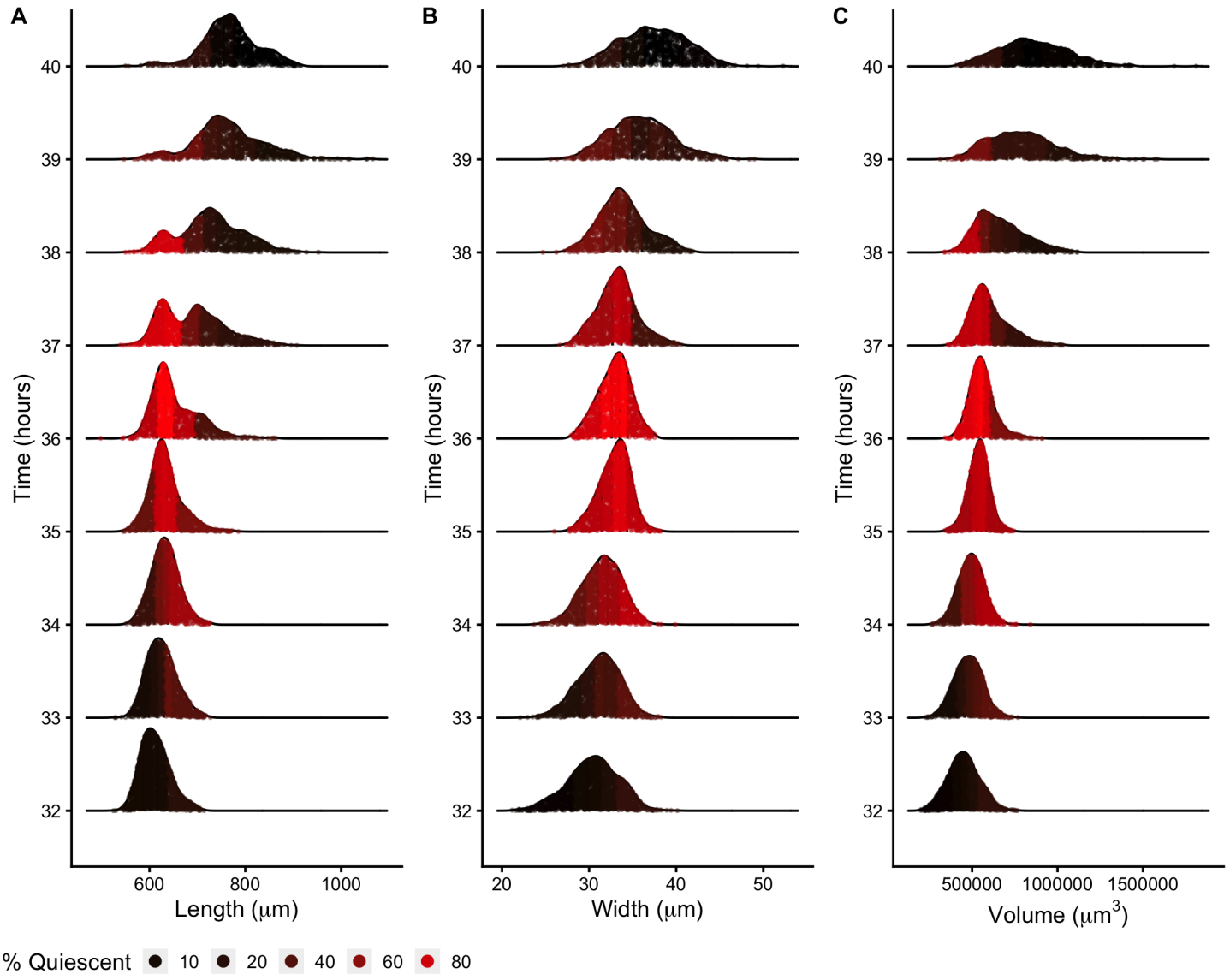

Fig 4. Density plots of population size dynamics during a single larval transition.

Population density curves of length (A), width (B) and volume (C) for the hours surrounding the L3 - L4 larval transition. Each distribution was divided into five quantiles. The percentage of quiescent animals present within each quantile was calculated (see Methods), and each quantile was colored to reflect this percentage. In all shape variables, quantiles that contain the largest animals displayed an increase in quiescence earlier than quantiles that contain the smallest animals. These dynamics were consistent across all larval-stage transitions (S7 Fig).

bioRxiv preprint doi: https://doi.org/10.1101/2021.04.01.438121; this version posted April 2, 2021. The copyright holder for this preprint (which was not certified by peer review) is the author/funder, who has granted bioRxiv a license to display the preprint in perpetuity. It is made available under aCC-BY 4.0 International license.

Cuticle stretch determines timing of larval-stage transitions

Previous studies theorized that the internal mechanism for sensing body size and triggering molts in *C. elegans* is driven, in part, by the properties of the collagen-rich cuticle [27]. Many cuticle collagen mutations cause morphological defects in nematode shape some of which cause animals to be shorter but do not impact animal width, implying that the cuticle affects length and width independently [53]. The *C. elegans* cuticle does not grow through the addition of new material, but rather stretches to accommodate increases in animal body size. Cuticle stretch is limited by the material properties of the cuticle. Previous work on *nekl-3(sv3)* mutants demonstrated that the cuticle can become sufficiently stiff to restrict *C. elegans* growth after a period of stretching [54]. These mutants are unable to shed the cuticle around the middle part of their body, restricting the size of the encased middle to pre-molt dimensions while the head and tail continue to grow normally. We hypothesize that *C. elegans* sense when the cuticle becomes restrictive and use a threshold in the reduction of elasticity or “stretchiness” of the cuticle to determine when to initiate molt.

To explain the initialization of molt behavior, we developed a “Stretcher” model for a cuticle-stretch-based threshold that triggers *C. elegans* larval-stage transitions. We propose that the nematode passes through three distinct regimes related to cuticle stretch: linear stretch dynamics, non-linear stretch dynamics, and larval stage transition (Fig 5). The cuticle structure is anisotropic, possibly leading to distinct properties in the length and width directions [55,56]. We approximated the cuticle as a hollow cylinder of negligible thickness filled by the body of the nematode. Growth is modelled as internal pressure evenly applied to the cuticle in all directions. The cuticle responds differently during linear stretch, nonlinear stretch, and post-molt relaxation.

bioRxiv preprint doi: https://doi.org/10.1101/2021.04.01.438121; this version posted April 2, 2021. The copyright holder for this preprint (which was not certified by peer review) is the author/funder, who has granted bioRxiv a license to display the preprint in perpetuity. It is made available under aCC-BY 4.0 International license.

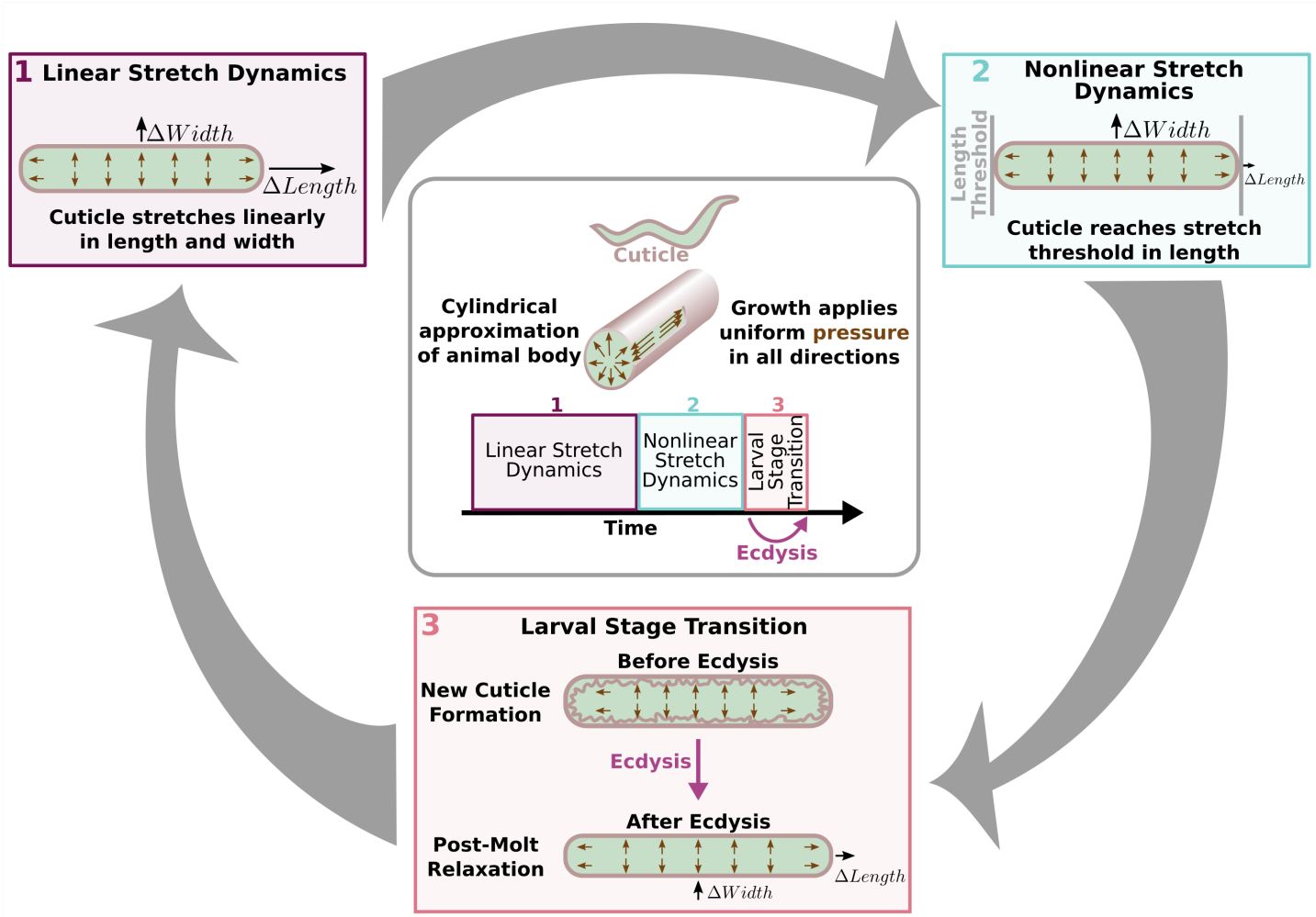

Fig 5. Cuticle stretch determines larval-stage transitions

The "Stretcher" model describes each larval stage as a cycle. Nematodes are modeled as a cylindrical object with a thin cuticle epidermis. (Box 1) Linear Stretch Dynamics: uniform growth pressure stretches the cuticle linearly in both length and width. (Box 2) Nonlinear Stretch Dynamics: Cuticle has reached a stretch threshold in length, and under uniform growth pressure the length stretches less (sub-linear) and width stretches linearly. (Box 3) Larval Stage Transition: a new cuticle is formed and the old cuticle is shed (ecdysis), removing constraints in length. The nematode body "relaxes" in length, causing an increase in length, a decrease in width, and constant volume.

In the linear stretch regime (Fig 5), the cuticle is linearly elastic in both the length and width directions, stretching proportionally to the pressure exerted on the cuticle. Previous work found evidence for a linearly

bioRxiv preprint doi: https://doi.org/10.1101/2021.04.01.438121; this version posted April 2, 2021. The copyright holder for this preprint (which was not certified by peer review) is the author/funder, who has granted bioRxiv a license to display the preprint in perpetuity. It is made available under aCC-BY 4.0 International license.

elastic cuticle [57,58] in animals expanded in a negative external pressure environment or after positive force was applied to the cuticle. A linearly elastic cuticle will have ΔL stretch in the length direction and ΔW stretch in the width direction, each related to growth-applied pressure Δp by

$$\Delta L = a_L \Delta p \quad (1)$$

$$\Delta W = a_W \Delta p \,. \quad (2)$$

The "stretch coefficients" in length, a_L, and width, a_W, measure the stiffness of the cuticle (S5 File, Eq. S14-S23). Smaller values correspond to a stiffer material, which is less able to stretch in response to pressure. The stretch coefficients are constant in the linearly elastic regime and are determined by geometric constants and material properties. The ratio of the change in length (Eq. 1) and width (Eq. 2) produces an experimentally verifiable, pressure-independent relationship that depends only on the ratio of the geometric and material properties. Eq. 9 predicts that during the linearly elastic regime, the ratio of growth in width to growth in length is constant throughout a larval stage where the cuticle properties are fixed.

$$\frac{\Delta W}{\Delta L} = \frac{a_W}{a_L} = constant \quad (3)$$

In the non-linear stretch regime (Fig 5), growth continues to apply pressure to the cuticle uniformly in all directions. As observed in *nekl-3(sv3)* mutants, the cuticle can become stiff when stretched beyond tolerance [54]. Once outside of the linearly elastic regime, the cuticle hardly stretches, even under large forces. We hypothesized that this shift from linear to nonlinear regimes provides a way for animals to sense their own size and cues the larval-stage transition (Fig 5). In principle, this transition could occur in either the width or length directions, or both, but our results are consistent with transitioning from linear to non-linear stretch in the length direction and maintaining linear stretch in the width direction (Fig 6). In the nonlinear regime, the stretch in the length direction in response to pressure becomes

bioRxiv preprint doi: https://doi.org/10.1101/2021.04.01.438121; this version posted April 2, 2021. The copyright holder for this preprint (which was not certified by peer review) is the author/funder, who has granted bioRxiv a license to display the preprint in perpetuity. It is made available under aCC-BY 4.0 International license.

$$\Delta L \approx \tilde{a}_L(p)\,\Delta p \quad (4)$$

The nonlinear "stretch coefficient," $\tilde{a}_L(p)$, is no longer constant and decreases with increasing pressure. It is smaller than a_L because the cuticle has become less elastic than in the linear regime. If the length-direction enters the nonlinear regime and has reduced stretch response, while width has the same constant stretch response then, we expect the $\frac{\Delta W}{\Delta L}$ ratio to increase

$$\frac{\Delta W}{\Delta L}\Big|_{non-linear} = \frac{a_W}{\tilde{a}_L(p)} > \frac{a_w}{a_L} = \frac{\Delta W}{\Delta L}\Big|_{linear} \quad (5)$$

During larval stage transition (Fig 5), a new, larger cuticle is formed beneath the old cuticle that is shed during ecdysis. Because the old cuticle constrained growth in length, we predict a rapid increase in the length direction when the constraint is removed. Nematode volume is conserved as growth does not occur during this process. Therefore, the relaxation in length is accompanied by a corresponding decrease in width.

bioRxiv preprint doi: https://doi.org/10.1101/2021.04.01.438121; this version posted April 2, 2021. The copyright holder for this preprint (which was not certified by peer review) is the author/funder, who has granted bioRxiv a license to display the preprint in perpetuity. It is made available under aCC-BY 4.0 International license.

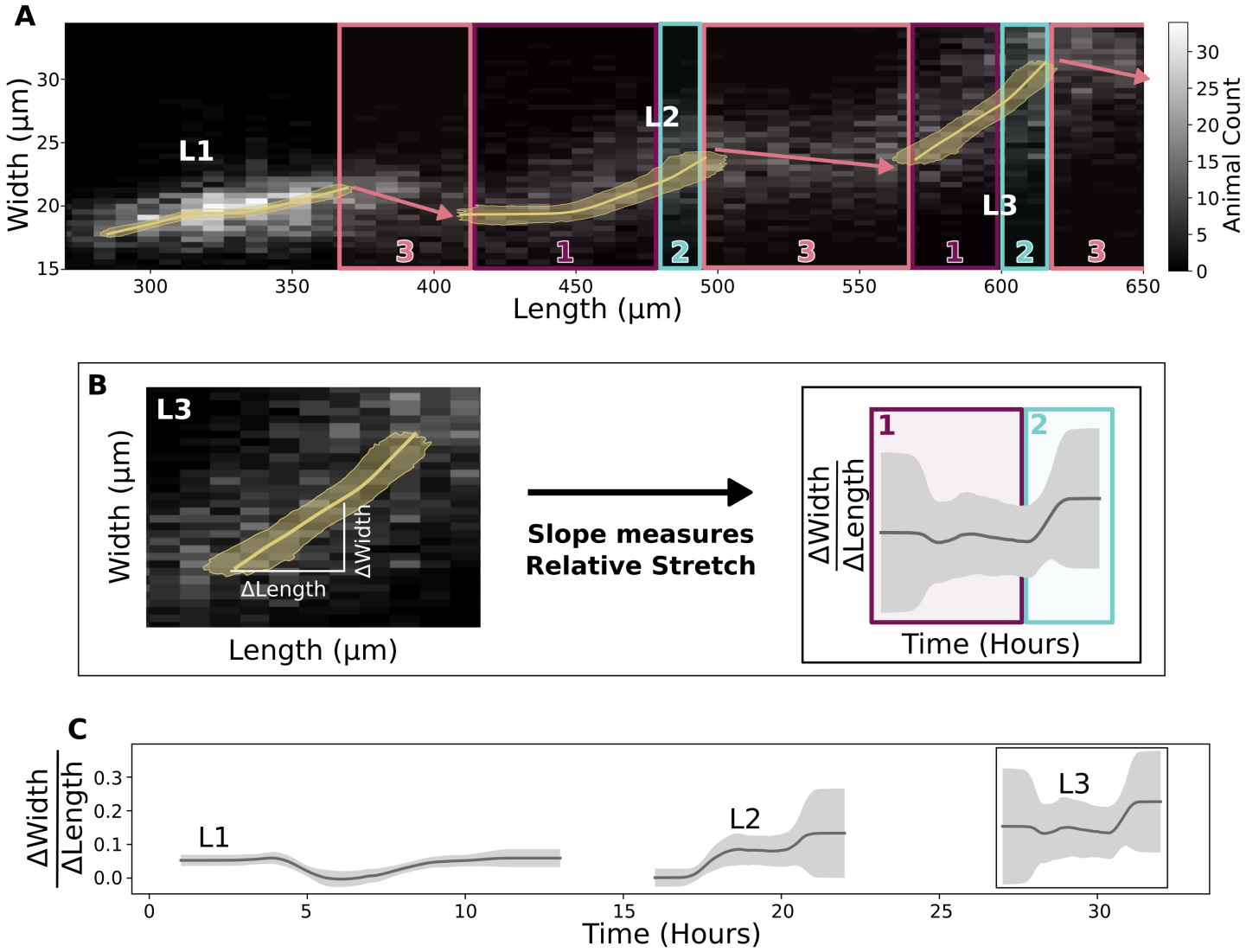

511 **Fig 6. Stretcher model analysis of replicate 2 COPAS BIOSORT data consistent with a length trigger for**
512 **molting**

513 (A) A grayscale histogram of the width (y-axis) vs length (x-axis) of all sampled animals in replicate 2. The
514 range of all bootstrap regressions is in gold. (B) The ratio of width to length stretch is the local slope. (C) Within
515 a larval stage, the ratio of width to length stretch varies over time. The standard deviation captures population
516 variation (grey) (S5 File, Eq. S26, S28).

517

518

519 To verify the shape dynamics predicted by the Stretcher model, we analyzed the relationship between
520 nematode length and width over developmental time. All three regimes, linear stretch, non-linear stretch, and

bioRxiv preprint doi: https://doi.org/10.1101/2021.04.01.438121; this version posted April 2, 2021. The copyright holder for this preprint (which was not certified by peer review) is the author/funder, who has granted bioRxiv a license to display the preprint in perpetuity. It is made available under aCC-BY 4.0 International license.

relaxation, predicted by the Stretcher model are detectable in the COPAS BIOSORT data (Fig 6). In all larval stages, the instantaneous ratio $\frac{\Delta W}{\Delta L}$ was approximately constant for the majority of the time, consistent with a linear stretch regime (Fig 6C). We observed a large slope decrease during the L1 stage, which could correspond in time to the metabolic decision for entry into the dauer stage [59]. Near the end of L2 and L3 stages, we observed a sharp slope increase, supporting our predictions of a non-linear stretch regime in length prior to lethargus. We note that the transitions between larval stages contain an increase in length and a decrease in width (Fig 6A and S8 Fig) consistent with a length threshold in the Stretcher model. These results suggest that the material properties of the cuticle, specifically the loss of ability to stretch in the length direction in response to pressure from growth, generate a mechanical signal for the start of larval transition.

Mechanical control of feeding and allocation of food constrain growth dynamics

We have shown that changes in physical properties of the *C. elegans* cuticle precede the decision to initiate molt and might serve as a cue for developmental timing. *C. elegans* must have mechanisms to control growth throughout development, particularly in response to these cues. Like most species, *C. elegans*, do not increase their growth rate indefinitely in response to increased food availability [27]. The animals could control growth entirely through feeding rate, as they actively control the feeding rate [60] and stop feeding at the initiation of a molt [22]. In addition to this mechanical control, they could use metabolic control to preemptively divert ingested resources toward or away from growth. Metabolic processing of stored resources could be especially useful if animals complete their molt and enter a food-limited environment. For these reasons, we investigated the possible mechanical control of feeding (Fig 7A) and the metabolic control of the allocation of ingested food toward organismal growth and development (Fig 8A). Using a quantitative feeding model, we calculated the rate of mechanical feeding behavior from volume and food intake data. Additionally, we distinguish when mechanical feeding rate or other regulatory mechanisms, such as metabolic control, are the primary drivers of growth rate during *C. elegans* development.

bioRxiv preprint doi: https://doi.org/10.1101/2021.04.01.438121; this version posted April 2, 2021. The copyright holder for this preprint (which was not certified by peer review) is the author/funder, who has granted bioRxiv a license to display the preprint in perpetuity. It is made available under aCC-BY 4.0 International license.

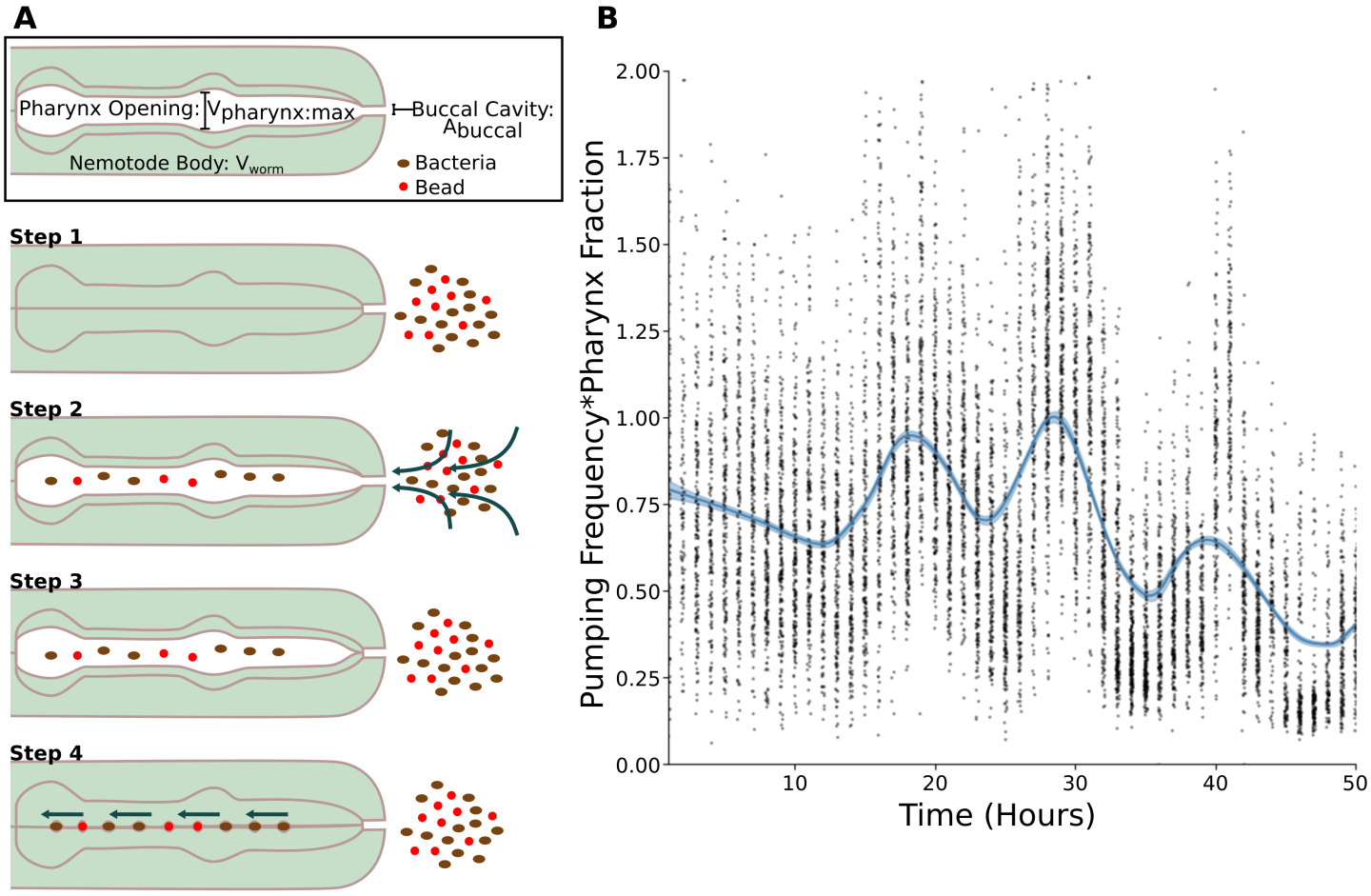

546

547 **Fig 7. Visualization and analysis of Feeding Model**

548 Schematics for food intake and utilization models are shown. (A) The buccal cavity is the opening through

549 which food enters. The pharynx is the cavity opened and closed by pharyngeal muscles that drives food intake.

550 (B) Product of pumping frequency and pharynx fraction, $f(t)g(t)$.

551

bioRxiv preprint doi: https://doi.org/10.1101/2021.04.01.438121; this version posted April 2, 2021. The copyright holder for this preprint (which was not certified by peer review) is the author/funder, who has granted bioRxiv a license to display the preprint in perpetuity. It is made available under aCC-BY 4.0 International license.

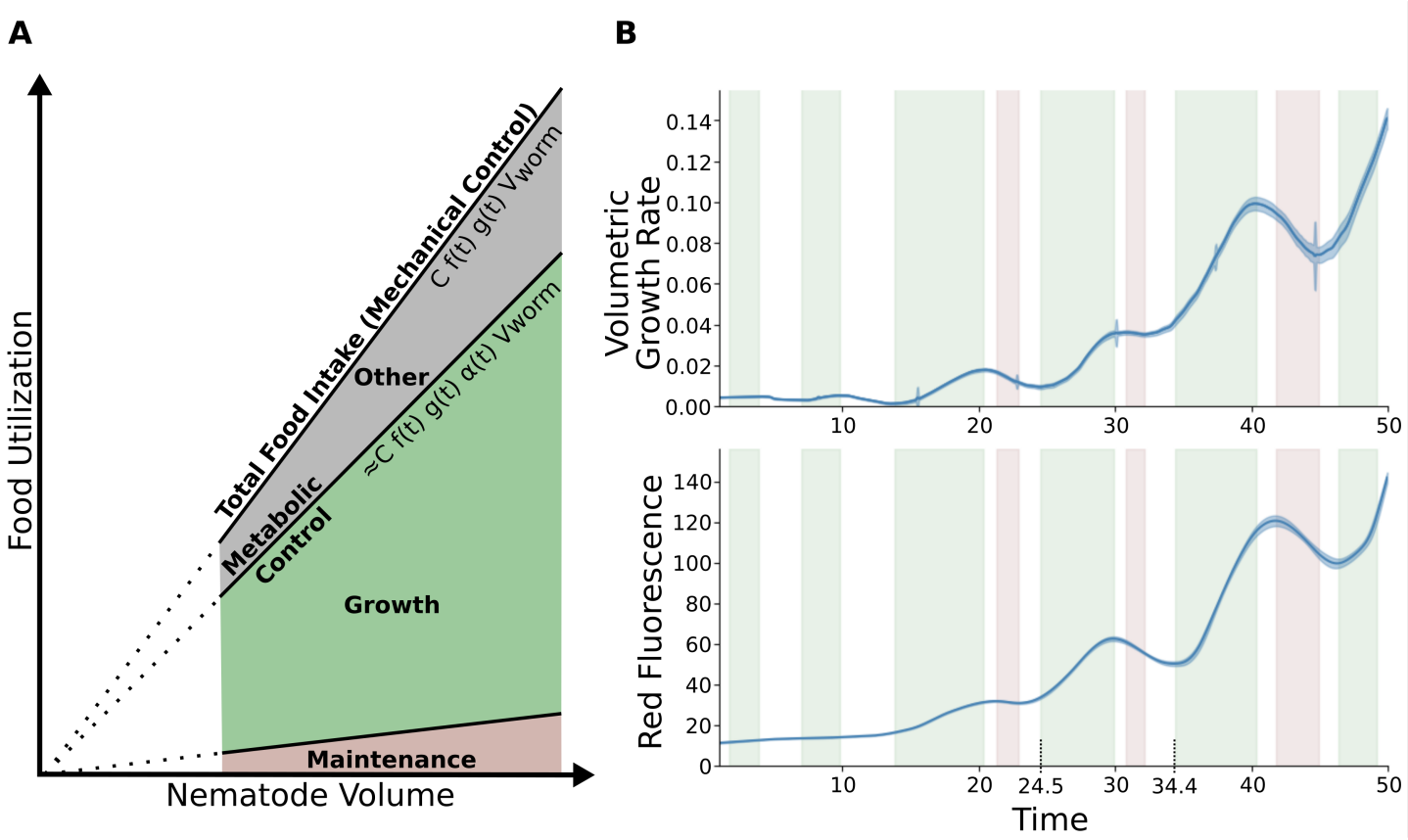

Fig 8. Visualization and analysis of Food Utilization model.

(A) The utilization of food resources as a function of animal volume. Total food intake controlled by feeding rate. Maintenance is assumed to be negligible. Metabolic control partitions food resources used for growth from other metabolic needs. (B) Dynamics of red fluorescence and volume growth rate. Errors on shaded regions are ±0.7 hours. These data are from replicate 2 and are representative of all replicates (S11 Fig).

Variation in pumping rate controls food uptake

C. elegans is a filter feeder that pumps its food through a cycle of pharyngeal muscle contractions and relaxations that alternatively open and close the pharyngeal cavity. *C. elegans* are capable of actively modulating the length of time used to contract or open a subset of the pharyngeal muscles [60]. Our feeding model describes how control of this pumping period translates to changes in the rate of food uptake.

bioRxiv preprint doi: https://doi.org/10.1101/2021.04.01.438121; this version posted April 2, 2021. The copyright holder for this preprint (which was not certified by peer review) is the author/funder, who has granted bioRxiv a license to display the preprint in perpetuity. It is made available under aCC-BY 4.0 International license.

A single pumping cycle in which animals take up and transport food to the gut consists of four general steps (Fig 7A). The cycle begins with relaxed pharyngeal muscles and a closed pharynx (step 1). The animal opens the pharynx so that fluid and food flow through the buccal cavity and into the pharynx (step 2). The animal cannot create a vacuum, so the volume of the cavity produced must be filled entirely by media and bacteria. The animal relaxes the muscles that control the opening, stopping the flow of fluid through the buccal cavity and trapping a volume of media approximately equal to the maximum volume of the pharynx (step 3). Finally, the pharynx closes, extruding excess media and trapping bacteria and beads that are then 'swallowed' (step 4). The period of a single cycle varies throughout the life cycle of *C. elegans* [60].

We find a relationship between eating rate and animal volume. It has previously been suggested that the cross-sectional area of the buccal cavity is a limiting factor in the rate of food intake [26]. However the volume of the pharynx is filled each pumping period so the pharynx volume, not the cross-sectional area, sets food uptake rate. We express pharynx volume as a fraction, $g(t)$, of nematode volume, $V_{pharynx:max}(t) = g(t) \cdot V_{worm}(t)$. As the pumping period is much faster (roughly 200 ms in adults) [60] than the rate of measured growth (hours), we averaged the food intake rate, $\frac{dV_{food}}{dt}$, over a single pumping period (S5 File, Eq. S1-S6) to obtain

$$\frac{dV_{food}}{dt} = Cf(t)g(t)V_{worm}. \quad (6)$$

Here $f(t)$ is the pumping frequency and the inverse of the period of a single pump. Both pumping frequency, $f(t)$, and the fractional pharynx size, $g(t)$, vary over the animal's life cycle.

By using red fluorescence as a proxy measurement for food intake rate and calculated volume we estimated the product of pumping rate and pharynx fraction, $f(t)g(t) \propto \frac{Red}{V_{worm}}$, over time. The product oscillated within a larval stage and decreased across larval stages (Fig 7B). The minima of the product of pumping frequency and

bioRxiv preprint doi: https://doi.org/10.1101/2021.04.01.438121; this version posted April 2, 2021. The copyright holder for this preprint (which was not certified by peer review) is the author/funder, who has granted bioRxiv a license to display the preprint in perpetuity. It is made available under aCC-BY 4.0 International license.

pharynx fraction occurred during molt times, consistent with prior knowledge [22,25]. Pharynx length has been shown to decrease over development [61] and a similar trend in pharynx volume could explain the slow decrease in the product of pumping frequency and pharynx fraction.

Changes in food utilization coincide with molts

To understand whether the mechanical feeding process or metabolic regulation is the primary driver of growth and development, we describe how food is utilized once it is ingested by *C. elegans*. We assumed three general categories of food utilization: maintenance, growth, and all other processes. We assumed that, when animals are not food restricted the maintenance resource requirement is negligible compared to the food utilized for growth. The rate of food conversion can be described by:

$$\frac{dV_{worm}(t)}{dt} = \eta(t)\alpha(t)\frac{dV_{food}}{dt}(t) \quad (7)$$

Here, $\frac{dV_{food}}{dt}$ is the instantaneous rate of food intake (averaged over a single pump), $\eta(t)$ is the metabolic efficiency of converting food to growth, and $\alpha(t)$ is the fraction of food used for growth as opposed to other metabolic processes. If $\eta(t)$ and $\alpha(t)$ are constant then Eq. (4) predicts the rate of volumetric growth is directly proportional to the rate of food consumption. If, instead, efficiency of food utilization or the fraction of food utilized for growth are not constant, then volumetric growth rate is no longer proportional to food consumption rate and metabolic or regulatory control must play a role in driving the growth rate.

Feeding rate (using red fluorescence as a proxy) and volume growth rate (numerically differentiated from the volume regression) are highly correlated throughout much of *C. elegans* development (Fig 8B). Each larval stage consists of three types of dynamics: steady growth during which food intake and growth rate are both increasing (green), preparation for molt during which food intake and growth rate are both decreasing (red), and transition regions where food intake and growth rate are uncorrelated (white). To illustrate how these dynamics correspond to the progression within a larval stage, consider the L3 larvae in replicate 2. At hour

bioRxiv preprint doi: https://doi.org/10.1101/2021.04.01.438121; this version posted April 2, 2021. The copyright holder for this preprint (which was not certified by peer review) is the author/funder, who has granted bioRxiv a license to display the preprint in perpetuity. It is made available under aCC-BY 4.0 International license.

24.5, both growth rate and food intake rate increased corresponding to the start of the third larval stage for the population average. Until hour 29.8, the population grew steadily, and food intake and growth rate both increased (green). Between hour 29.8 and 30.8 (white), food intake decreased and growth rate increased, marking a transition from the steady growth (green) to the molt preparation regime (red). Between hours 30.8 and 32.1, the animals prepared to initiate molts, and both the growth rate and food intake rate decreased (red). Between hours 32.1 and 34.4 (white), the animals' growth rate increased once again while the food intake rate continued to decrease corresponding to the end of the molt and start of the L4 larval stage. Similar dynamics occurred in the L2 and L3 larval stages. The L1 larval stage followed different dynamics, likely due to the dauer decision.

During steady growth (green) and molt initiation (red), it is likely that growth is controlled by the rate of food intake and thus under mechanical control by the animal. Loss of correlation between growth rate and food intake rate (white) implies food intake rate can no longer be the primary driver of changes in growth rate. Either the efficiency of metabolism, captured by $\eta(t)$, or the resource allocation toward growth, captured by $\alpha(t)$, must vary at these times. In either case, the lack of correlation before and after each molt suggests other regulatory mechanisms must be at play during these times.

Feeding rate and volumetric growth rate share a complex relationship with *C. elegans* development; food intake and growth rate are highly correlated, except at larval stage transitions and possible key developmental transitions. Notably, the metabolic decision indicated by the transition from increasing to decreasing growth and food intake rates (Fig 8B) occurred at approximately the same times as the increase in slope predicted as a cue for molt initiation by the Stretcher model (Fig 6). This correlation suggests that the cuticle reaches its maximum stretch in length and a metabolic decision to reallocate food resources growth occurs at the same time. This result supports the hypothesis that a physical threshold in stretch triggers metabolic decisions to enter a molt (S10 Fig).

bioRxiv preprint doi: https://doi.org/10.1101/2021.04.01.438121; this version posted April 2, 2021. The copyright holder for this preprint (which was not certified by peer review) is the author/funder, who has granted bioRxiv a license to display the preprint in perpetuity. It is made available under aCC-BY 4.0 International license.

Discussion

Using an integrated image-based and flow-based phenotyping strategy to precisely evaluate feeding, growth, and molt dynamics at high replication, we detected oscillations in feeding behavior consistent with larval progressions and used these dynamics to define larval stages. We observed changes in body shape at each larval-stage transition that are consistent with differences in physical cuticle properties along length or width (anisotropy). These results suggest that animals sense their size and control molt timing by detecting the physical stretch of the cuticle. To understand whether C elegans control growth through moderating the physical uptake of nutrients or through metabolic regulation of the allocation of consumed resources we applied mathematical models of feeding-limited growth to our data. We predicted that volumetric growth rate was primarily controlled by *C. elegans* feeding rate for most of development, yet at molts and during a period of the L1 larval stage, other regulatory processes drive growth. These results demonstrate two mechanisms by which physical constraints can influence developmental timing and growth rate.

Cuticle stretch controls the timing of larval-stage transitions

Measurement of both animal length and width allowed us to observe changes in body shape as well as body size. We propose that a “Stretch threshold” along the body length axis acts as a trigger to larval-stage transitions. For cuticle stretch to trigger larval-stage transitions, animals must either have the ability to measure the amount the cuticle has stretched or the stiffness of the cuticle. Across biological systems, cells can respond to the stiffness of their environment using mechanosensitive components [62,63], but few examples in tissues or whole-organisms are known. In *C. elegans*, it has been demonstrated that hemidesmosomes, which connect the cuticle and the epidermis, are mechanosensitive during embryogenesis [64,65]. Additionally, dense bodies, which connect the epidermis and muscles, are hypothesized to be mechanosensitive as well ([24,66–68]. Changes in cuticle composition, and presumably stiffness, have been shown to also affect well known growth controlling pathways such as the BMP signaling pathway [69]. These possible mechanosensitive components could monitor the stiffness of the cuticle and be part of the signaling pathways that regulate

bioRxiv preprint doi: https://doi.org/10.1101/2021.04.01.438121; this version posted April 2, 2021. The copyright holder for this preprint (which was not certified by peer review) is the author/funder, who has granted bioRxiv a license to display the preprint in perpetuity. It is made available under aCC-BY 4.0 International license.

larval-stage transitions. Further experiments are required to explicitly test whether these components control larval-stage transitions.

Our analysis of width-to-length ratio variation over larval stages provides a first approximation of the timing of larval-stage transition cues and cuticle stretch properties (Fig 8). The sudden increase we observed in the width-to-length ratio suggests a length stretch threshold. Single-worm, high frequency measurements targeting hours surrounding the sudden width-to-length ratio increase, are needed to better resolve cuticle shape dynamics. Higher time resolution would also minimize edge effects (S12 Fig), which likely caused the unpredicted width-to-length ratio increase observed at the start of larval stage L2 (Fig 8C). Measurements of animal length and width provide a total stiffness estimate but do not allow us to distinguish the contributions of cuticle stiffness from other tissues. To investigate cuticle properties, independent of other nematode tissues and organs, experiments must probe the stiffness of free cuticles.

Physical constraints on feeding influence growth dynamics

Our mechanical feeding model defines a relationship between food availability, food intake rate, food utilization, and growth rate. We distinguished between food intake rate and pumping rates by modeling the physical process of feeding. The results of our analysis are consistent with both an oscillation in pumping rates [22] and a slow change in pharynx size throughout development [61]. Previous research suggested that pumping frequencies within a larval stage are constant with sudden transitions between lethargus and pumping [51]. However, we were unable to resolve sudden transitions because of the continuous smoothing of the kernel regression method used and population effects (Fig 7B). Previous work has shown that growth rate increases with increasing food availability up to a saturation limit [27]. Varying bacterial concentration levels in future experiments would allow us to distinguish whether mechanical control of food intake or metabolic control of food utilization determine the upper bound on growth rate.

bioRxiv preprint doi: https://doi.org/10.1101/2021.04.01.438121; this version posted April 2, 2021. The copyright holder for this preprint (which was not certified by peer review) is the author/funder, who has granted bioRxiv a license to display the preprint in perpetuity. It is made available under aCC-BY 4.0 International license.

Our analysis of the relationship between growth rate and food intake rate demonstrated short periods of time during which growth rate and food intake rate were not correlated. These periods may be developmental points in which metabolic decisions are being made and food and energy resource allocation is changing. Within the L2 and L3 stages we observed a loss of correlation between growth rate and food intake twice. The first of these time periods corresponds to the times at which the width-to-length ratio drastically changes and the second corresponds to ecdysis (S10 Fig). The loss of correlation between growth and food intake motivates the need for further metabolomic experiments to probe metabolic regulation surrounding larval stage transitions.

In the analysis of both the Stretcher and feeding models, we found that the L1 larval stage has different dynamics than other larval stages. We observed a decrease in growth rate with no associated decrease in feeding rate, corresponding to a mid-stage resource reallocation, that does not occur in any other larval stage, possibly showing the dauer decision [59]. Additionally, within the L1 stage, the relative stretch measured in width and length did not follow the pattern observed in other larval stages. We observed a mid-stage dip in the width-to-length ratio that is otherwise approximately constant throughout the L1 stage. As animals reallocate food resources around the dauer decision, they also undergo a change in shape suggesting either directed growth or structural changes to either the cuticle or animal body during L1 (Fig 3, Fig 6, S8 Fig). Future experiments exploring the structural properties of cuticles at all larval stages may help to determine where the L1 shape changes originate.

Metazoan development comprises complex interactions of growth regulation across diverse scales

Our results demonstrate that *C. elegans* uses physical constraints on animal size and feeding rate to control growth rate and determine developmental transitions. The control of whole-organism growth requires cells, tissues, and organs to orchestrate final size and cell number. In *C. elegans*, cell number is precisely defined and invariant from animal to animal [70], so the final adult size of an individual must come from cell size as opposed to number. Future studies should focus on how whole-organism size is determined by the integration

bioRxiv preprint doi: https://doi.org/10.1101/2021.04.01.438121; this version posted April 2, 2021. The copyright holder for this preprint (which was not certified by peer review) is the author/funder, who has granted bioRxiv a license to display the preprint in perpetuity. It is made available under aCC-BY 4.0 International license.

718 of cell, tissue, and organ size. By incorporating these different developmental scales, the Stretcher model can
719 be refined to completely describe how physical constraints on parts of the organism impact the whole. *C.*
720 *elegans* gives investigators a method to investigate animal-to-animal variation in developmental trajectories
721 across each of these scales.

722

bioRxiv preprint doi: https://doi.org/10.1101/2021.04.01.438121; this version posted April 2, 2021. The copyright holder for this preprint (which was not certified by peer review) is the author/funder, who has granted bioRxiv a license to display the preprint in perpetuity. It is made available under aCC-BY 4.0 International license.

References

1. Hone DWE, Benton MJ. The evolution of large size: how does Cope's Rule work? Trends Ecol Evol. 2005;20: 4–6.

2. Björklund M. Cell size homeostasis: Metabolic control of growth and cell division. Biochim Biophys Acta Mol Cell Res. 2019;1866: 409–417.

3. Willis L, Huang KC. Sizing up the bacterial cell cycle. Nat Rev Microbiol. 2017;15: 606–620.

4. Turner JJ, Ewald JC, Skotheim JM. Cell size control in yeast. Curr Biol. 2012;22: R350–9.

5. Donnan L, John PC. Cell cycle control by timer and sizer in Chlamydomonas. Nature. 1983;304: 630–633.

6. Wang P, Hayden S, Masui Y. Transition of the blastomere cell cycle from cell size-independent to size-dependent control at the midblastula stage in Xenopus laevis. J Exp Zool. 2000;287: 128–144.

7. Tzur A, Kafri R, LeBleu VS, Lahav G, Kirschner MW. Cell growth and size homeostasis in proliferating animal cells. Science. 2009;325: 167–171.

8. Pavelescu I, Vilarrasa-Blasi J, Planas-Riverola A, González-García M-P, Caño-Delgado AI, Ibañes M. A Sizer model for cell differentiation in Arabidopsis thaliana root growth. Mol Syst Biol. 2018;14: e7687.

9. Sveiczer A, Novak B, Mitchison JM. The size control of fission yeast revisited. J Cell Sci. 1996;109 (Pt 12): 2947–2957.

10. Campos M, Surovtsev IV, Kato S, Paintdakhi A, Beltran B, Ebmeier SE, et al. A constant size extension drives bacterial cell size homeostasis. Cell. 2014;159: 1433–1446.

11. Taheri-Araghi S, Bradde S, Sauls JT, Hill NS, Levin PA, Paulsson J, et al. Cell-size control and homeostasis in bacteria. Curr Biol. 2015;25: 385–391.

12. Soifer I, Robert L, Amir A. Single-Cell Analysis of Growth in Budding Yeast and Bacteria Reveals a

bioRxiv preprint doi: https://doi.org/10.1101/2021.04.01.438121; this version posted April 2, 2021. The copyright holder for this preprint (which was not certified by peer review) is the author/funder, who has granted bioRxiv a license to display the preprint in perpetuity. It is made available under aCC-BY 4.0 International license.

744 Common Size Regulation Strategy. Curr Biol. 2016;26: 356–361.

745 13. Osella M, Nugent E, Cosentino Lagomarsino M. Concerted control of Escherichia coli cell division. Proc
746 Natl Acad Sci U S A. 2014;111: 3431–3435.

747 14. Jorgensen P, Tyers M. How cells coordinate growth and division. Curr Biol. 2004;14: R1014–27.

748 15. Wang P, Robert L, Pelletier J, Dang WL, Taddei F, Wright A, et al. Robust growth of Escherichia coli. Curr
749 Biol. 2010;20: 1099–1103.

750 16. Cadart C, Monnier S, Grilli J, Sáez PJ, Srivastava N, Attia R, et al. Size control in mammalian cells
751 involves modulation of both growth rate and cell cycle duration. Nat Commun. 2018;9: 3275.

752 17. Moss-Taylor L, Upadhyay A, Pan X, Kim M-J, O'Connor MB. Body Size and Tissue-Scaling Is Regulated
753 by Motoneuron-Derived Activinß in Drosophila melanogaster. Genetics. 2019;213: 1447–1464.

754 18. Spence AJ. Scaling in biology. Curr Biol. 2009;19: R57–61.

755 19. Uppaluri S, Weber SC, Brangwynne CP. Hierarchical Size Scaling during Multicellular Growth and
756 Development. Cell Rep. 2016;17: 345–352.

757 20. Wood WB. The Nematode Caenorhabditis Elegans. Cold Spring Harbor Laboratory; 1988.

758 21. Page AP, Johnstone IL. The cuticle. WormBook. 2007; 1–15.

759 22. Singh RN, Sulston JE. Some Observations On Moulting in Caenorhabditis Elegans. Nematologica.
760 1978;24: 63–71.

761 23. Monsalve GC, Van Buskirk C, Frand AR. LIN-42/PERIOD controls cyclical and developmental progression
762 of C. elegans molts. Curr Biol. 2011;21: 2033–2045.

763 24. Zaidel-Bar R, Miller S, Kaminsky R, Broday L. Molting-specific downregulation of C. elegans body-wall
764 muscle attachment sites: the role of RNF-5 E3 ligase. Biochem Biophys Res Commun. 2010;395:

bioRxiv preprint doi: https://doi.org/10.1101/2021.04.01.438121; this version posted April 2, 2021. The copyright holder for this preprint (which was not certified by peer review) is the author/funder, who has granted bioRxiv a license to display the preprint in perpetuity. It is made available under aCC-BY 4.0 International license.

509–514.

25. Byerly L, Cassada RC, Russell RL. The life cycle of the nematode Caenorhabditis elegans. I. Wild-type growth and reproduction. Dev Biol. 1976;51: 23–33.

26. Knight CG, Patel MN, Azevedo RBR, Leroi AM. A novel mode of ecdysozoan growth in Caenorhabditis elegans. Evol Dev. 2002;4: 16–27.

27. Uppaluri S, Brangwynne CP. A size threshold governs Caenorhabditis elegans developmental progression. Proc Biol Sci. 2015;282: 20151283.

28. Tuck S. The control of cell growth and body size in Caenorhabditis elegans. Exp Cell Res. 2014;321: 71–76.

29. Patterson GI, Padgett RW. TGF beta-related pathways. Roles in Caenorhabditis elegans development. Trends Genet. 2000;16: 27–33.

30. McKeown C, Praitis V, Austin J. sma-1 encodes a betaH-spectrin homolog required for Caenorhabditis elegans morphogenesis. Development. 1998;125: 2087–2098.

31. Madaan U, Yzeiraj E, Meade M, Clark JF, Rushlow CA, Savage-Dunn C. BMP Signaling Determines Body Size via Transcriptional Regulation of Collagen Genes in Caenorhabditis elegans. Genetics. 2018;210: 1355–1367.

32. Page AP, Johnstone IL. The cuticle. WormBook; 2007.

33. Baugh LR. To grow or not to grow: nutritional control of development during Caenorhabditis elegans L1 arrest. Genetics. 2013;194: 539–555.

34. Hu PJ. Dauer. WormBook; 2018.

35. Mörck C, Pilon M. C. elegans feeding defective mutants have shorter body lengths and increased

bioRxiv preprint doi: https://doi.org/10.1101/2021.04.01.438121; this version posted April 2, 2021. The copyright holder for this preprint (which was not certified by peer review) is the author/funder, who has granted bioRxiv a license to display the preprint in perpetuity. It is made available under aCC-BY 4.0 International license.

786 autophagy. BMC Dev Biol. 2006;6: 39.

787 36. Cook DE, Zdraljevic S, Tanny RE, Seo B, Riccardi DD, Noble LM, et al. The Genetic Basis of Natural
788 Variation in Caenorhabditis elegans Telomere Length. Genetics. 2016;204: 371–383.

789 37. Andersen EC, Bloom JS, Gerke JP, Kruglyak L. A variant in the neuropeptide receptor npr-1 is a major
790 determinant of Caenorhabditis elegans growth and physiology. PLoS Genet. 2014;10: e1004156.

791 38. Stiernagle T. Maintenance of C. elegans. WormBook; 2006.

792 39. Abràmoff MD, Magalhães PJ, Ram SJ. Image processing with ImageJ. Biophotonics international.
793 2004;11: 36–42.

794 40. Andersen EC, Shimko TC, Crissman JR, Ghosh R, Bloom JS, Seidel HS, et al. A Powerful New
795 Quantitative Genetics Platform, Combining Caenorhabditis elegans High-Throughput Fitness Assays with
796 a Large Collection of Recombinant Strains. G3 . 2015;5: 911–920.

797 41. Shimko TC, Andersen EC. COPASutils: An R Package for Reading, Processing, and Visualizing Data from
798 COPAS Large-Particle Flow Cytometers. PLoS ONE. 2014. p. e111090. doi:10.1371/journal.pone.0111090

799 42. Scrucca L, Fop M, Murphy TB, Raftery AE. mclust 5: Clustering, Classification and Density Estimation
800 Using Gaussian Finite Mixture Models. R J. 2016;8: 289–317.

801 43. Smith MV, Boyd WA, Kissling GE, Rice JR, Snyder DW, Portier CJ, et al. A discrete time model for the
802 analysis of medium-throughput C. elegans growth data. PLoS One. 2009;4: e7018.

803 44. Hermann E. lokern: Kernel Regression Smoothing with Local or Global Plug-in Bandwidth. R package
804 version 1.1-8. 2016. Available: https://CRAN.R-project.org/package=lokern

805 45. Sakamoto Y, Ishiguro M, Kitagawa G. Akaike information criterion statistics. Dordrecht, The Netherlands:
806 D Reidel. 1986;81: 26853.

bioRxiv preprint doi: https://doi.org/10.1101/2021.04.01.438121; this version posted April 2, 2021. The copyright holder for this preprint (which was not certified by peer review) is the author/funder, who has granted bioRxiv a license to display the preprint in perpetuity. It is made available under aCC-BY 4.0 International license.

807 46. Schwarz G. Estimating the Dimension of a Model. aos. 1978;6: 461–464.

808 47. Kass RE, Raftery AE. Bayes Factors. J Am Stat Assoc. 1995;90: 773.

809 48. Burnham KP, Anderson DR. Model Selection and Multimodel Inference: A Practical Information-Theoretic
810 Approach. Springer Science & Business Media; 2007.

811 49. Lokern: Kernel regression smoothing with local or global plug-in bandwidth. [cited 16 Mar 2021]. Available:
812 https://CRAN.R-project.org/package=lokern

813 50. Cassada RC, Russell RL. The dauerlarva, a post-embryonic developmental variant of the nematode
814 Caenorhabditis elegans. Dev Biol. 1975;46: 326–342.

815 51. Nika L, Gibson T, Konkus R, Karp X. Fluorescent Beads Are a Versatile Tool for Staging Caenorhabditis
816 elegans in Different Life Histories. G3 . 2016;6: 1923–1933.

817 52. Vuaridel-Thurre G, Vuaridel AR, Dhar N, McKinney JD. Computational Analysis of the Mutual Constraints
818 between Single-Cell Growth and Division Control Models. Adv Biosyst. 2020;4: e1900103.

819 53. Brenner S. The genetics of Caenorhabditis elegans. Genetics. 1974;77: 71–94.

820 54. Yochem J, Lažetić V, Bell L, Chen L, Fay D. C. elegans NIMA-related kinases NEKL-2 and NEKL-3 are
821 required for the completion of molting. Dev Biol. 2015;398: 255–266.

822 55. Petzold BC, Park S-J, Ponce P, Roozeboom C, Powell C, Goodman MB, et al. Caenorhabditis elegans
823 body mechanics are regulated by body wall muscle tone. Biophys J. 2011;100: 1977–1985.

824 56. Cox GN, Staprans S, Edgar RS. The cuticle of Caenorhabditis elegans. II. Stage-specific changes in
825 ultrastructure and protein composition during postembryonic development. Dev Biol. 1981;86: 456–470.

826 57. Park S-J, Goodman MB, Pruitt BL. Analysis of nematode mechanics by piezoresistive displacement
827 clamp. Proc Natl Acad Sci U S A. 2007;104: 17376–17381.

bioRxiv preprint doi: https://doi.org/10.1101/2021.04.01.438121; this version posted April 2, 2021. The copyright holder for this preprint (which was not certified by peer review) is the author/funder, who has granted bioRxiv a license to display the preprint in perpetuity. It is made available under aCC-BY 4.0 International license.

58. Gilpin W, Uppaluri S, Brangwynne CP. Worms under Pressure: Bulk Mechanical Properties of C. elegans Are Independent of the Cuticle. Biophysical Journal. 2015. pp. 1887–1898. doi:10.1016/j.bpj.2015.03.020

59. Golden JW, Riddle DL. The Caenorhabditis elegans dauer larva: developmental effects of pheromone, food, and temperature. Dev Biol. 1984;102: 368–378.

60. Fang-Yen C, Avery L, Samuel ADT. Two size-selective mechanisms specifically trap bacteria-sized food particles in Caenorhabditis elegans. Proc Natl Acad Sci U S A. 2009;106: 20093–20096.

61. Avery L. Food transport in the C. elegans pharynx. Journal of Experimental Biology. 2003. pp. 2441–2457. doi:10.1242/jeb.00433

62. Schiller HB, Fässler R. Mechanosensitivity and compositional dynamics of cell-matrix adhesions. EMBO Rep. 2013;14: 509–519.

63. Wolfenson H, Bershadsky A, Henis YI, Geiger B. Actomyosin-generated tension controls the molecular kinetics of focal adhesions. J Cell Sci. 2011;124: 1425–1432.

64. Suman SK, Daday C, Ferraro T, Vuong-Brender T, Tak S, Quintin S, et al. The plakin domain of VAB-10/plectin acts as a hub in a mechanotransduction pathway to promote morphogenesis. Development. 2019;146. doi:10.1242/dev.183780

65. Zhang H, Landmann F, Zahreddine H, Rodriguez D, Koch M, Labouesse M. A tension-induced mechanotransduction pathway promotes epithelial morphogenesis. Nature. 2011;471: 99–103.

66. Moerman DG, Williams BD. Sarcomere assembly in C. elegans muscle. WormBook. 2006; 1–16.

67. Costa M, Draper BW, Priess JR. The role of actin filaments in patterning the Caenorhabditis elegans cuticle. Dev Biol. 1997;184: 373–384.

68. Broday L, Hauser CA, Kolotuev I, Ronai Z 'ev. Muscle-epidermis interactions affect exoskeleton patterning in Caenorhabditis elegans. Dev Dyn. 2007;236: 3129–3136.

bioRxiv preprint doi: https://doi.org/10.1101/2021.04.01.438121; this version posted April 2, 2021. The copyright holder for this preprint (which was not certified by peer review) is the author/funder, who has granted bioRxiv a license to display the preprint in perpetuity. It is made available under aCC-BY 4.0 International license.

69. Madaan U, Faure L, Chowdhury A, Ahmed S, Ciccarelli EJ, Gumienny TL, et al. Feedback regulation of BMP signaling by cuticle collagens. Mol Biol Cell. 2020;31: 825–832.

70. Horvitz HR, Sulston JE. Isolation and genetic characterization of cell-lineage mutants of the nematode Caenorhabditis elegans. Genetics. 1980;96: 435–454.

bioRxiv preprint doi: https://doi.org/10.1101/2021.04.01.438121; this version posted April 2, 2021. The copyright holder for this preprint (which was not certified by peer review) is the author/funder, who has granted bioRxiv a license to display the preprint in perpetuity. It is made available under aCC-BY 4.0 International license.

Supporting Information Captions

S1 Fig. Raw measurements of animal size. Raw COPAS BIOSORT data of animal length (A), width (B), and volume (C) are shown here. Smaller objects observed after 65 hours were the next generation of newly hatched L1 larvae laid by the animals that developed during the time course.

S2 Fig. Correlation analysis of body size measurements. Manual measurements of animal length, width, and estimated area were compared to COPAS BIOSORT measurements of TOF, norm.EXT, and EXT. Kendall correlation value is shown in each plot.

S3 Fig. Mixture modeling of COPAS BIOSORT data was used to prune data. Mixture models of gaussian distributions were fit to log transformed animal length (x-axis) and log transformed optical extinction (y-axis). Data from each hour of the experiment was analyzed and processed to remove clusters that did not include animal objects. All replicates were pruned independently; a subset of data from replicate 2 is shown here. Panels indicate experimental hours from which data is taken.

S4 Fig. Fluorescence measurements normalized by body size. Red fluorescence beads were fed to animals during experimentation and fluorescence data was collected by the COPAS BIOSORT. Fluctuations in fluorescence indicate fluctuations in feeding behavior. Fluorescence data was normalized by body size measurements to account for increases in body size. Dividing fluorescence by area was most successful in normalizing fluorescence dynamics to account for changes in animal size over time.

S5 Fig. Cuticles identified during periods of decreased feeding. Images of wells collected during the experiment were examined for evidence of shed cuticles. (A) Experimental hours where cuticles were identified from images overlap with hours where population feeding behavior is low. Cuticles shed from the L4-Adult molt persisted longer than previous larval stage cuticle debri. (B) Example image of animal without visible cuticle during a period of elevated feeding. (C) Example image of an animal with visible cuticle indicating completion of molt during a period of decreased feeding.

S6 Fig. Volume growth data fit with linear, exponential, and cubic models. Volume data of individuals in time points defined as growth periods are analyzed for each stage. L1 stage was further separated into two periods to account for the volume dip that occurs mid-stage.

bioRxiv preprint doi: https://doi.org/10.1101/2021.04.01.438121; this version posted April 2, 2021. The copyright holder for this preprint (which was not certified by peer review) is the author/funder, who has granted bioRxiv a license to display the preprint in perpetuity. It is made available under aCC-BY 4.0 International license.

S7 Fig. Density plots of population size dynamics across all larval transitions. Density curves of length (A), width (B) and volume (C). Curves are divided into five quantiles and colored by the percentage of quiescent animals present within that quantile. Molts are estimated to occur at experimental hours 14, 25, 36, and 48 (see Methods).

S8 Fig. Animals in all replicates, measured from images. Animal length and width over C. elegans development captured from image data. Higher noise levels in these measurements preclude accurate regressions to individual larval stages. Length jumps and width dips are still apparent. Compare with Fig 6**.**

S9 Fig. Comparison of red fluorescence regression and food intake rate with defecation calculation. Regression of red fluorescence (dashed pink) is compared to the intake rate of red beads accounting for defecation rate (blue). Overlap of these two curves validates the use of red fluorescence as a proxy for food

S10 Fig. Timeline of Food Utilization and Stretcher events. In the first row (grey and white) we mark the slopes determined in the Stretcher model. Transition from lighter to darker grey indicates a step increase in slope corresponding to a stiffening cuticle in the length direction. White regions denote time between larval stages. L2 and L3 are the only stages at which we have useful slope information due to the dauer decision in L1 making transitions difficult to determine and the high level of population desynchronization in L4. In the second row (green, red, and white) we mark the food and growth correlations found in (Fig 5B). Green corresponds to times at which both growth rate and food rate are increasing. Red corresponds to times at which both growth rate and food rate are decreasing. White corresponds to times at which growth rate and food rate are uncorrelated. Transitions from green to red regions occur at roughly the same times as the transition to a stiffer cuticle in the length direction.

S11 Fig. Analysis of Food intake and growth rate correlation for all replicates. Summary of analysis in Fig. 8 for all replicates. Until larval stage L4, most replicates follow the same pattern of transitions from one growth regime to the next. The time delay at transitions in later replicates can be explained by the temperature gradient and differences in growth between replicates.

S12 Fig. Stretcher model analysis of replicate 2 COPAS BIOSORT data for different stage thresholding. Compare to Fig 5**.** Larval hours defined by taking the ceiling of the lower boundary and the floor of the upper

bioRxiv preprint doi: https://doi.org/10.1101/2021.04.01.438121; this version posted April 2, 2021. The copyright holder for this preprint (which was not certified by peer review) is the author/funder, who has granted bioRxiv a license to display the preprint in perpetuity. It is made available under aCC-BY 4.0 International license.

boundary. This rounding method for larval stage definition demonstrates the sensitivity of the analysis to edge effects. The unexpected step in the L2 larval stage (Fig 5) is significantly reduced with this rounding method.

S13 Fig. Sensitivity analysis to moving average window size. Varying lengths of window sizes (0.14 to 2.16 hours) were calculated for the *lokern* growth rate regression. Window size was increased until the growth rate regression was smoothed. A window size of 1.44 hours (or 0.72 hours on either side of each time point) was chosen to calculate the start and end times of each regime (Fig 8). Continued increase of window size past 1.44 hours did not change the pattern of regimes or their boundaries significantly.

S1 Table. Results of analysis of variance models fit to COPAS BIOSORT data. Analysis of variance tests were used to quantify the amount of variance in our data contributed by the sampling technique. The sampling technique involved unbiased sampling of animals from six replicate populations and subsequent distribution into multiple wells of a microtiter plate for analysis. We quantified the amount of variance contributed by replicate and well. We find that the variance explained by well is nearly negligible whereas replicate contributes minor variance in some measurements. Given this information, we deem the generated summary statistics an appropriate representation of the population.

S2 Table. Model fit criteria used to assess candidate growth models. To determine the level of support for each model, the candidate model with the smallest raw AIC/BIC was identified and compared to other AIC/BIC values. If the delta value was greater than 6, the model with the smallest AIC/BIC value was denoted as the best model. If the delta value was less than 6 but greater than 2, the model with the smallest AIC/BIC value was determined to likely be the best model. If the delta value was less than 2, we are unable to distinguish the model of best fit.

S1 File. Incubator temperature data. Temperature recordings of each position within the shaking incubator used for growth experiment. (CSV)

S2 File. COPAS BIOSORT growth data. Raw growth data collected from the COPAS BIOSORT and processed using the *easysorter* R package to compile information from each well. (CSV)

bioRxiv preprint doi: https://doi.org/10.1101/2021.04.01.438121; this version posted April 2, 2021. The copyright holder for this preprint (which was not certified by peer review) is the author/funder, who has granted bioRxiv a license to display the preprint in perpetuity. It is made available under aCC-BY 4.0 International license.

S3 File. Pruned COPAS BIOSORT growth data. Processed data from the COPAS BIOSORT following implementation of the *mclust* R package and removal of clusters containing non-animal objects. (CSV)

S4 File. Image growth data. Manual measurements of animal size acquired from images. (CSV)

S5 File. Model derivations.

bioRxiv preprint doi: https://doi.org/10.1101/2021.04.01.438121; this version posted April 2, 2021. The copyright holder for this preprint (which was not certified by peer review) is the author/funder, who has granted bioRxiv a license to display the preprint in perpetuity. It is made available under aCC-BY 4.0 International license.

Supporting Information Figures

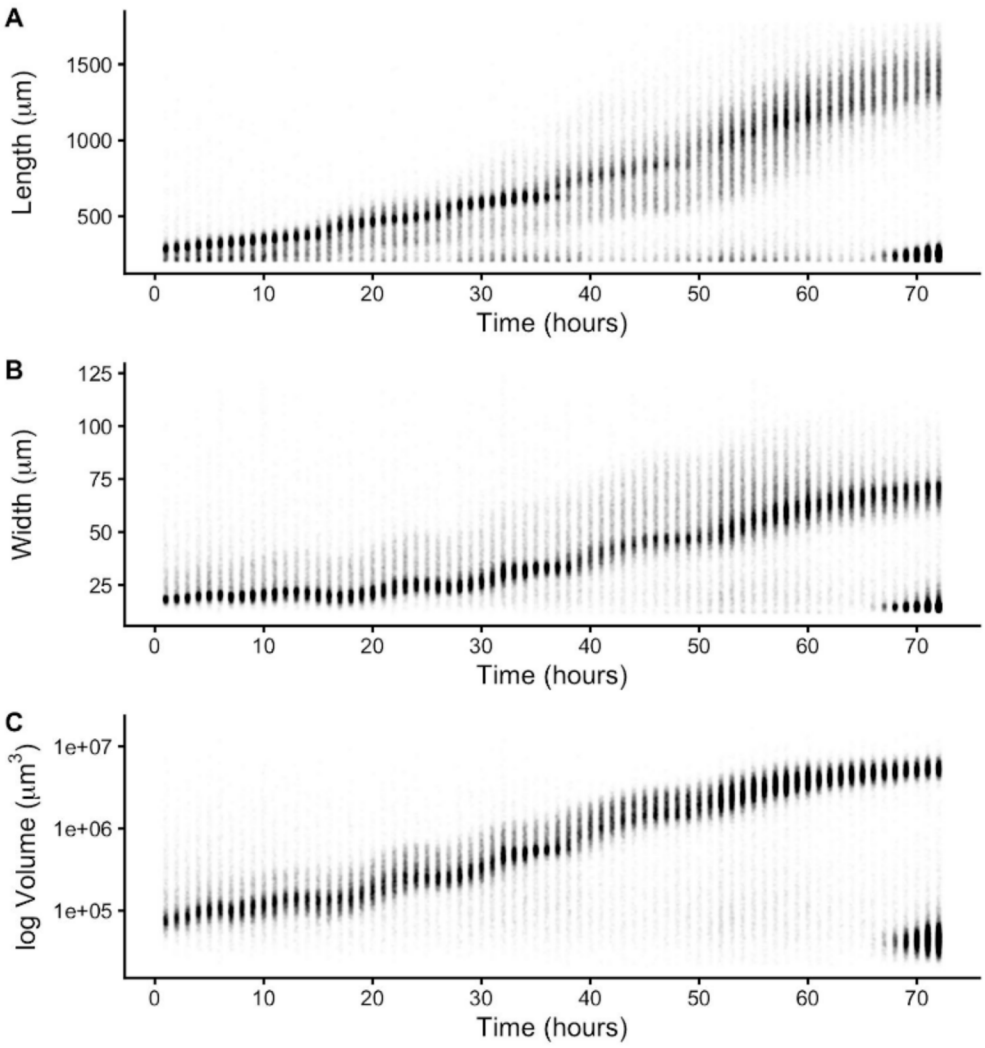

S1 Fig. Raw measurements of animal size. Raw COPAS BIOSORT data of animal length (A), width (B), and volume (C) are shown here. Smaller objects observed after 65 hours were the next generation of newly hatched L1 larvae laid by the animals that developed during the time course.

bioRxiv preprint doi: https://doi.org/10.1101/2021.04.01.438121; this version posted April 2, 2021. The copyright holder for this preprint (which was not certified by peer review) is the author/funder, who has granted bioRxiv a license to display the preprint in perpetuity. It is made available under aCC-BY 4.0 International license.

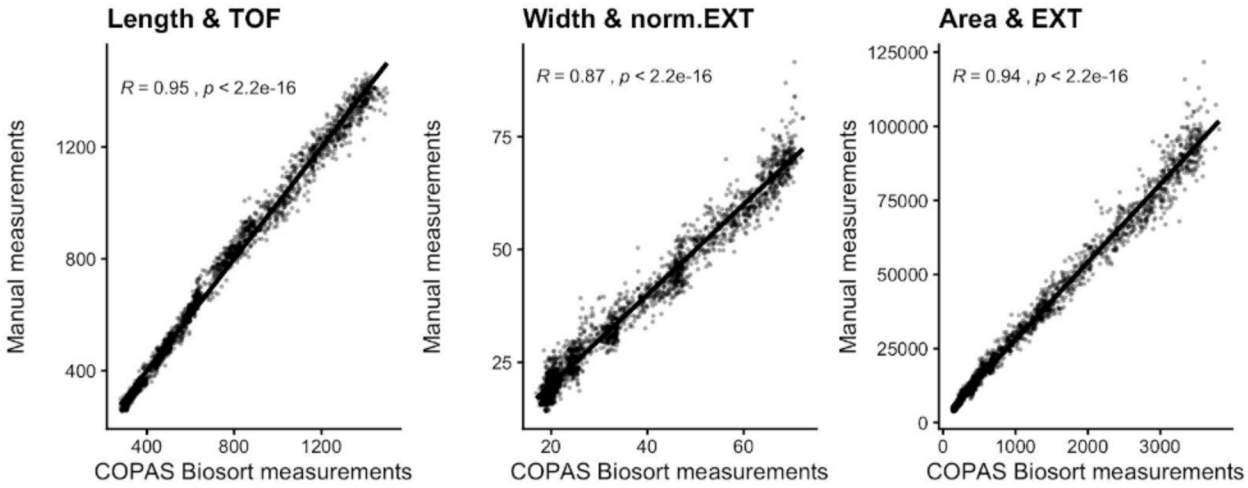

S2 Fig. Correlation analysis of body size measurements. Manual measurements of animal length, width, and estimated area were compared to COPAS BIOSORT measurements of TOF, norm.EXT, and EXT. Kendall correlation value is shown in each plot.

bioRxiv preprint doi: https://doi.org/10.1101/2021.04.01.438121; this version posted April 2, 2021. The copyright holder for this preprint (which was not certified by peer review) is the author/funder, who has granted bioRxiv a license to display the preprint in perpetuity. It is made available under aCC-BY 4.0 International license.

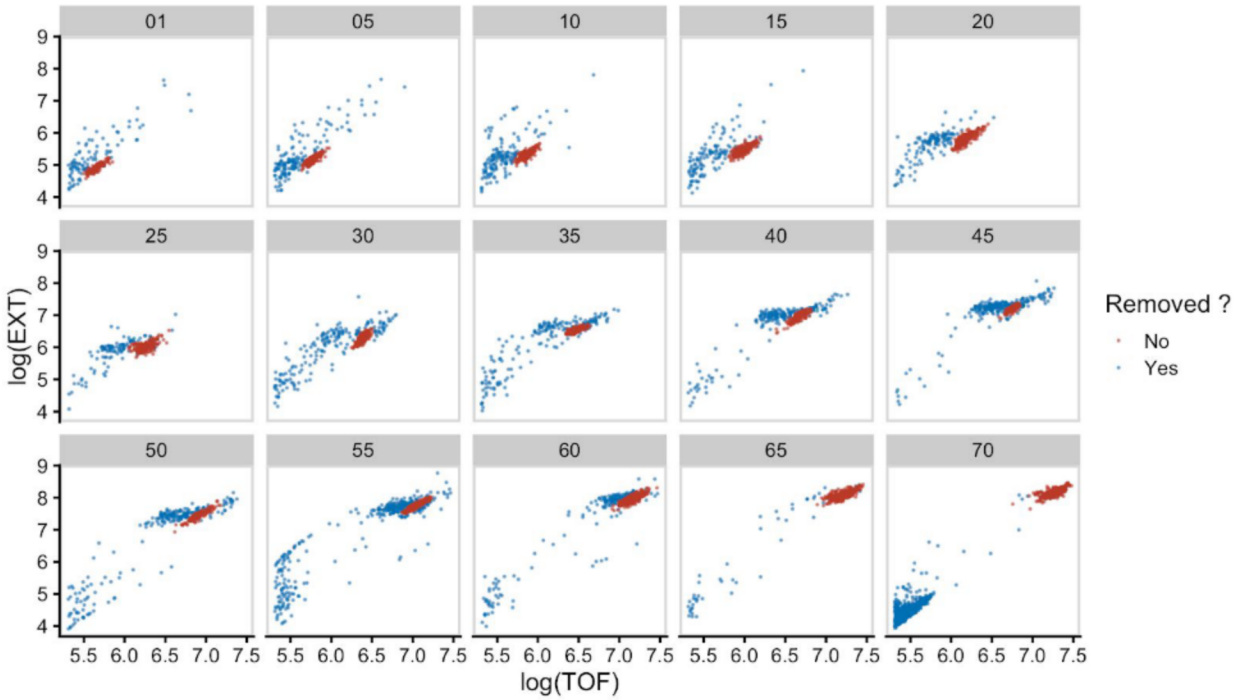

S3 Fig. Mixture modeling of COPAS BIOSORT data was used to prune data. Mixture models of gaussian distributions were fit to log transformed animal length (x-axis) and log transformed optical extinction (y-axis). Data from each hour of the experiment was analyzed and processed to remove clusters that did not include animal objects. All replicates were pruned independently; a subset of data from replicate 2 is shown here. Panels indicate experimental hours from which data is taken.

bioRxiv preprint doi: https://doi.org/10.1101/2021.04.01.438121; this version posted April 2, 2021. The copyright holder for this preprint (which was not certified by peer review) is the author/funder, who has granted bioRxiv a license to display the preprint in perpetuity. It is made available under aCC-BY 4.0 International license.

S1 Table. Results of analysis of variance models fit to COPAS BIOSORT data. Analysis of variance tests were used to quantify the amount of variance in our data contributed by the sampling technique. The sampling technique involved unbiased sampling of animals from six replicate populations and subsequent distribution into multiple wells of a microtiter plate for analysis. We quantified the amount of variance contributed by replicate and well. We find that the variance explained by well is nearly negligible whereas replicate contributes minor variance in some measurements. Given this information, we deem the generated summary statistics an appropriate representation of the population.

Response = Norm.Red

Terms	*Df*	*Sum Sq*	*Mean Sq*	*F value*	*Pr(>F)*	*% Var Explained*
hour	1	439.46	439.46	217762.01	0	54.34
replicate	6	165.82	27.64	13694.48	0	20.51
well	10	0.32	0.03	15.62	0	0.04
Residuals	100619	203.06	0	NA	NA	25.11

Response = Length

Terms	*Df*	*Sum Sq*	*Mean Sq*	*F value*	*Pr(>F)*	*% Var Explained*
hour	1	86190107879	86190107879	8223506	0	98.4
replicate	6	349438944	58239824	5557	0	0.4
well	10	834970	83497	8	0	0
Residuals	100619	1054582098	10481	NA	NA	1.2

Response = Width

Terms	*Df*	*Sum Sq*	*Mean Sq*	*F value*	*Pr(>F)*	*% Var Explained*
hour	1	209090438.47	209090438.47	6950760.3	0	97.99
replicate	6	1266985.87	211164.31	7019.7	0	0.59
well	10	1495.32	149.53	4.97	0	0
Residuals	100619	3026786.99	30.08	NA	NA	1.42

Response = Volume

Terms	*Df*	*Sum Sq*	*Mean Sq*	*F value*	*Pr(>F)*	*% Var Explained*
hour	1	621712474191714688	621712474191714688	843342	0	84.08
replicate	6	43356968850687072	7226161475114512	9802	0	5.86
well	10	152458715405862	15245871540586	21	0	0.02
Residuals	100619	74176459811167296	737201321929	NA	NA	10.03

bioRxiv preprint doi: https://doi.org/10.1101/2021.04.01.438121; this version posted April 2, 2021. The copyright holder for this preprint (which was not certified by peer review) is the author/funder, who has granted bioRxiv a license to display the preprint in perpetuity. It is made available under aCC-BY 4.0 International license.

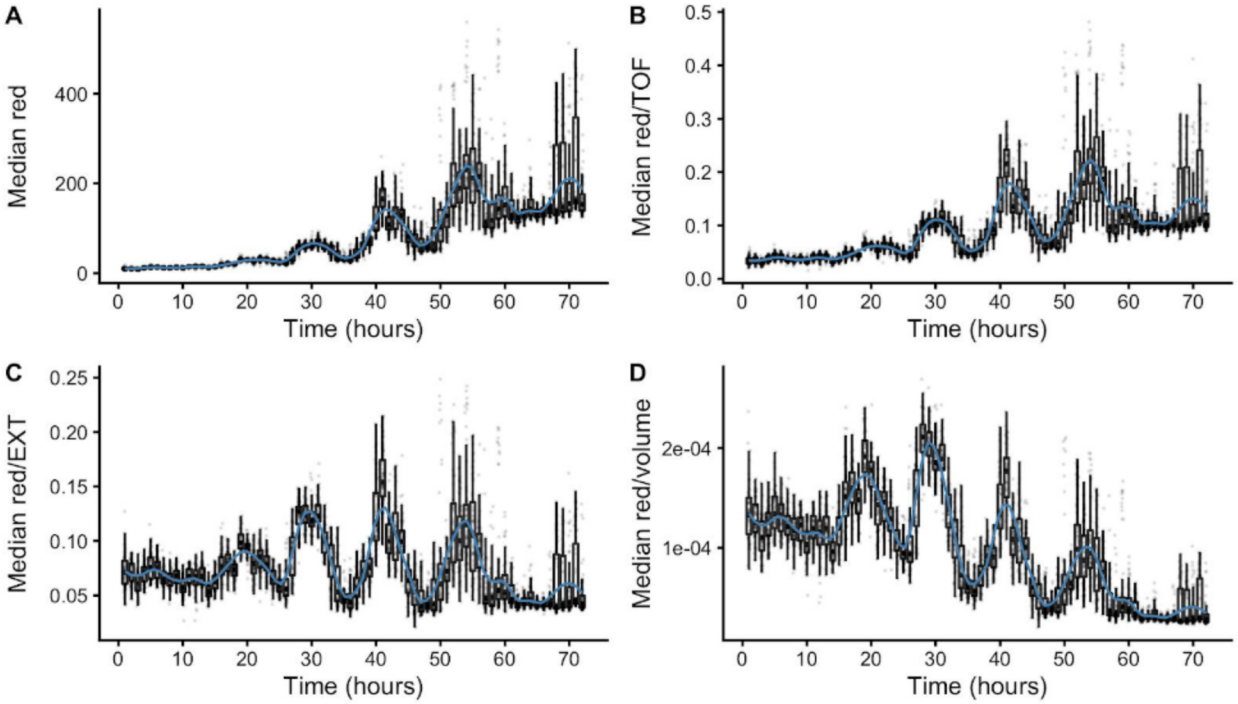

S4 Fig. Fluorescence measurements normalized by body size. Red fluorescence beads were fed to animals during experimentation and fluorescence data was collected by the COPAS BIOSORT. Fluctuations in fluorescence indicate fluctuations in feeding behavior. Fluorescence data was normalized by body size measurements to account for increases in body size. Dividing fluorescence by area was most successful in normalizing fluorescence dynamics to account for changes in animal size over time.

bioRxiv preprint doi: https://doi.org/10.1101/2021.04.01.438121; this version posted April 2, 2021. The copyright holder for this preprint (which was not certified by peer review) is the author/funder, who has granted bioRxiv a license to display the preprint in perpetuity. It is made available under aCC-BY 4.0 International license.

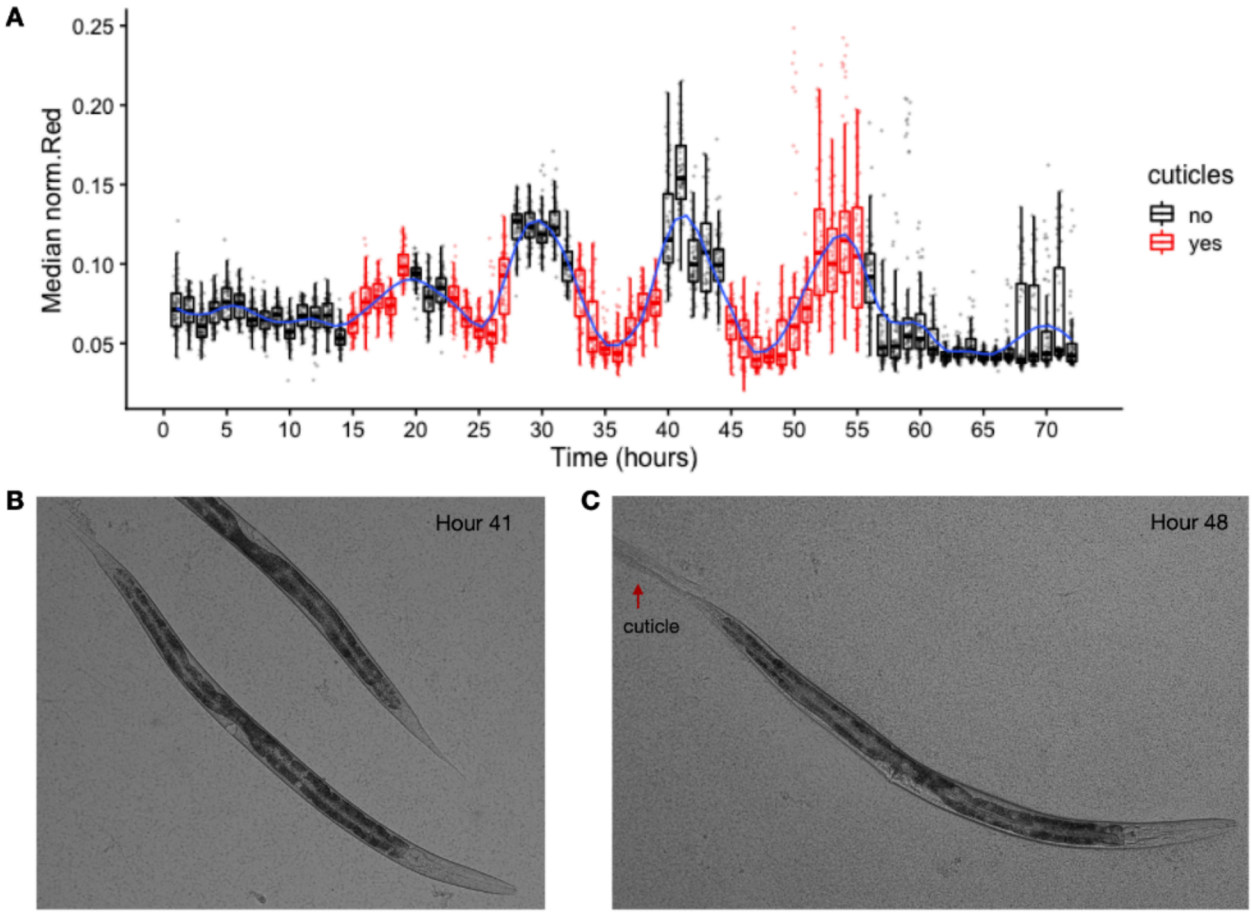

S5 Fig. Cuticles identified during periods of decreased feeding. Images of wells collected during the experiment were examined for evidence of shed cuticles. (A) Experimental hours where cuticles were identified from images overlap with hours where population feeding behavior is low. Cuticles shed from the L4-Adult molt persisted longer than previous larval stage cuticle debri. (B) Example image of animal without visible cuticle during a period of elevated feeding. (C) Example image of an animal with visible cuticle indicating completion of molt during a period of decreased feeding.

bioRxiv preprint doi: https://doi.org/10.1101/2021.04.01.438121; this version posted April 2, 2021. The copyright holder for this preprint (which was not certified by peer review) is the author/funder, who has granted bioRxiv a license to display the preprint in perpetuity. It is made available under aCC-BY 4.0 International license.

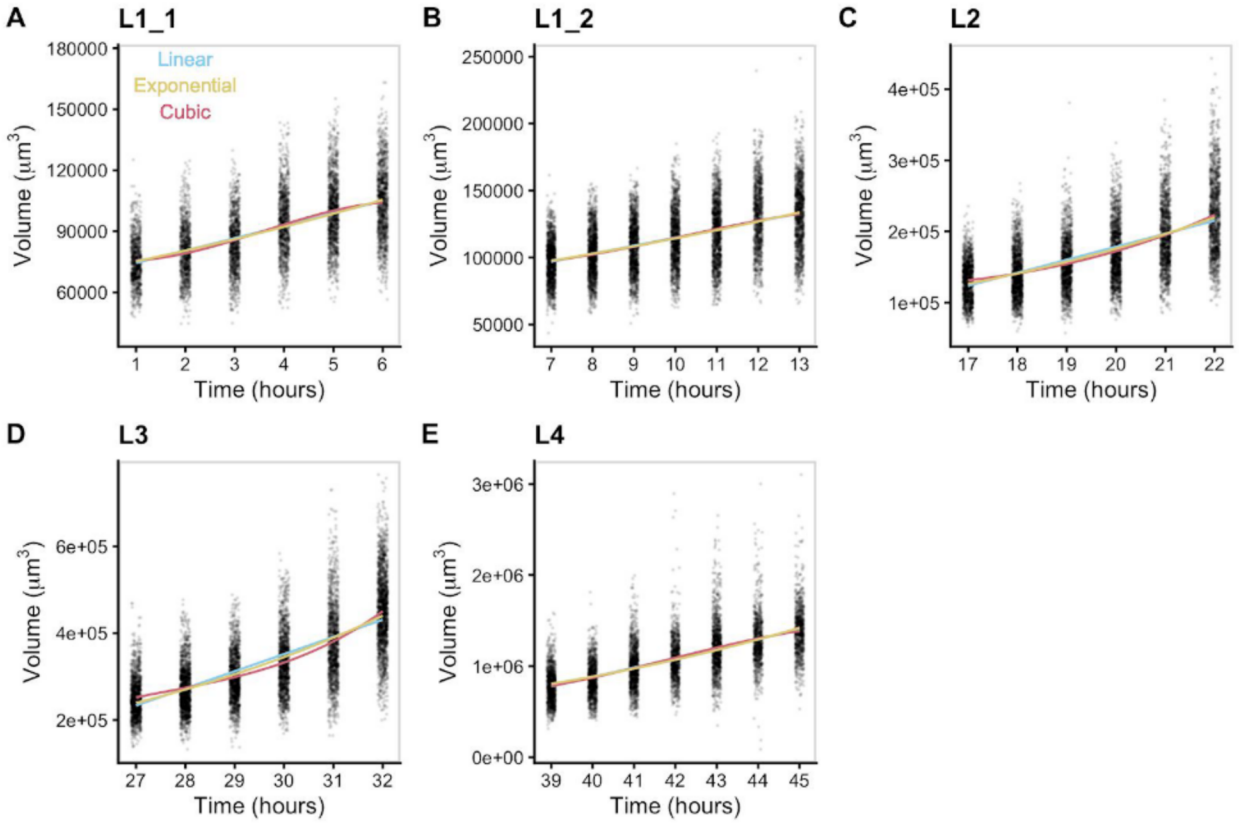

S6 Fig. Volume growth data fit with linear, exponential, and cubic models. Volume data of individuals in time points defined as growth periods are analyzed for each stage. L1 stage was further separated into two periods to account for the volume dip that occurs mid-stage.

bioRxiv preprint doi: https://doi.org/10.1101/2021.04.01.438121; this version posted April 2, 2021. The copyright holder for this preprint (which was not certified by peer review) is the author/funder, who has granted bioRxiv a license to display the preprint in perpetuity. It is made available under aCC-BY 4.0 International license.

S2 Table. Model fit criteria used to assess candidate growth models. To determine the level of support for each model, the candidate model with the smallest raw AIC/BIC was identified and compared to other AIC/BIC values. If the delta value was greater than 6, the model with the smallest AIC/BIC value was denoted as the best model. If the delta value was less than 6 but greater than 2, the model with the smallest AIC/BIC value was determined to likely be the best model. If the delta value was less than 2, we are unable to distinguish the model of best fit.

	ΔAIC			ΔBIC				
Stage	Linear	Exponential	Cubic	Linear	Exponential	Cubic	Best model by AIC	Best model by BIC
L1_1	17	21	0	4	9	0	Cubic	Likely Cubic
L1_2	2	4	0	0	2	12	Can't distinguish	Can't distinguish
L2	142	43	0	128	28	0	Cubic	Cubic
L3	374	145	0	360	131	0	Cubic	Cubic
L4	4	44	0	0	40	10	Likely Cubic	Linear

bioRxiv preprint doi: https://doi.org/10.1101/2021.04.01.438121; this version posted April 2, 2021. The copyright holder for this preprint (which was not certified by peer review) is the author/funder, who has granted bioRxiv a license to display the preprint in perpetuity. It is made available under aCC-BY 4.0 International license.

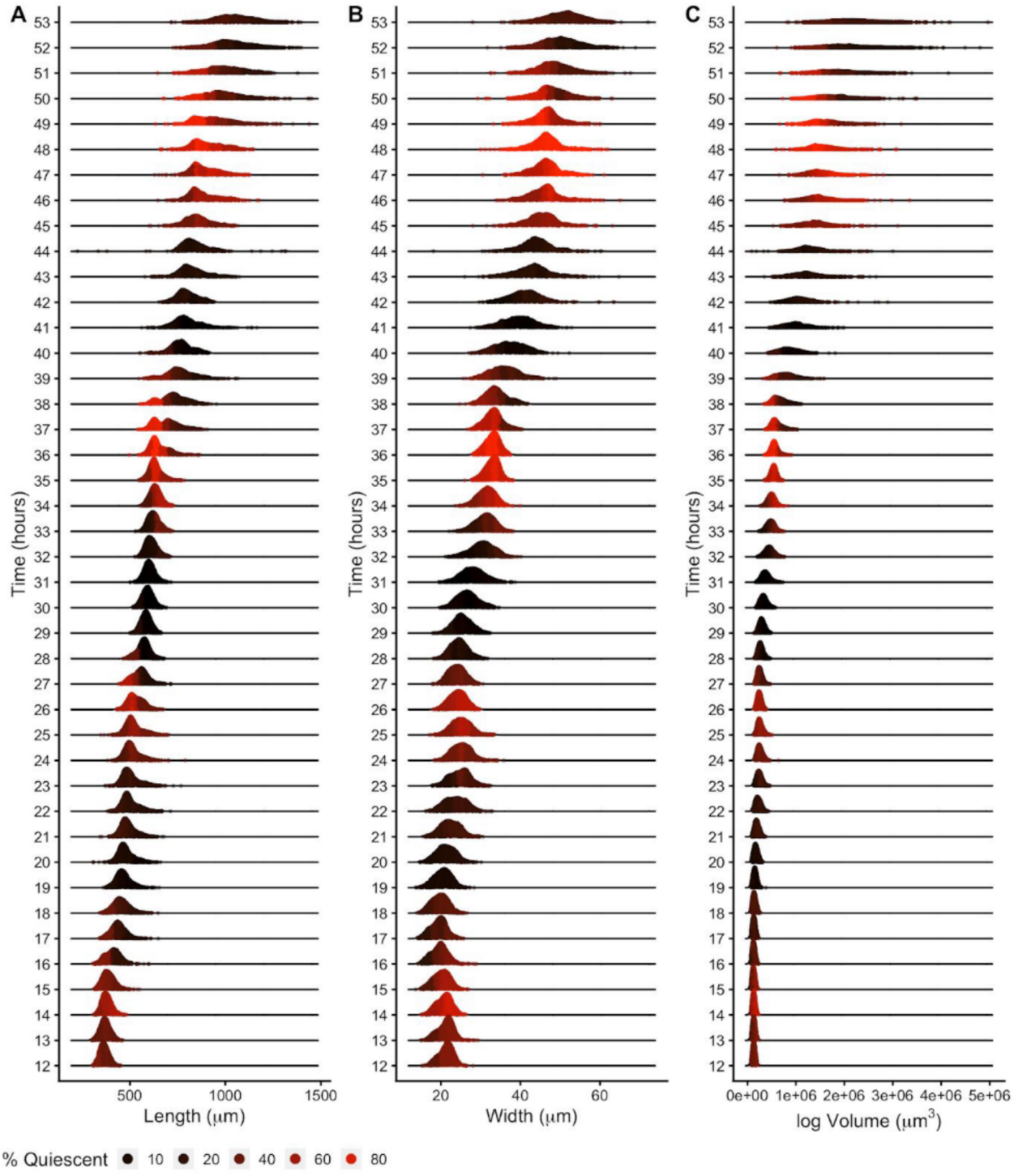

S7 Fig. Density plots of population size dynamics across all larval transitions. Density curves of length (A), width (B) and volume (C). Curves are divided into five quantiles and colored by the percentage of quiescent animals present within that quantile. Molts are estimated to occur at experimental hours 14, 25, 36, and 48 (see Methods).

bioRxiv preprint doi: https://doi.org/10.1101/2021.04.01.438121; this version posted April 2, 2021. The copyright holder for this preprint (which was not certified by peer review) is the author/funder, who has granted bioRxiv a license to display the preprint in perpetuity. It is made available under aCC-BY 4.0 International license.

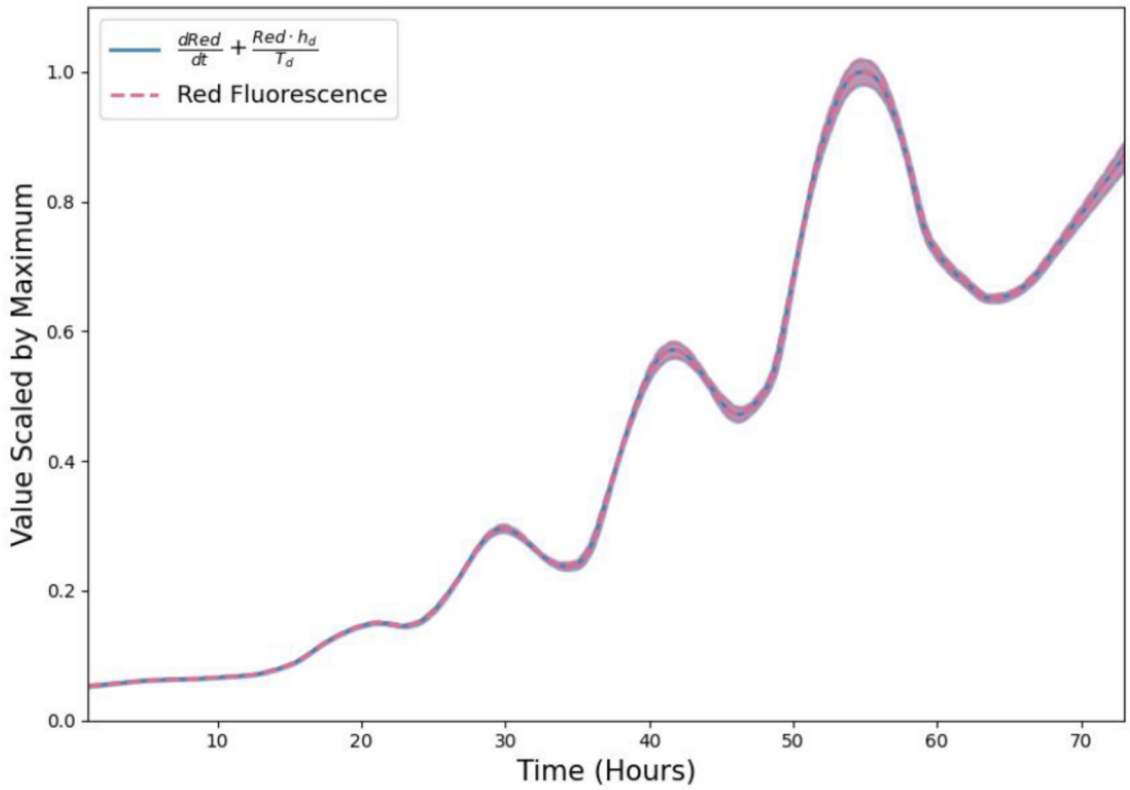

S9 Fig. Comparison of red fluorescence regression and food intake rate with defecation calculation

Regression of red fluorescence (dashed pink) is compared to the intake rate of red beads accounting for defecation rate (blue). Overlap of these two curves validates the use of red fluorescence as a proxy for food.

bioRxiv preprint doi: https://doi.org/10.1101/2021.04.01.438121; this version posted April 2, 2021. The copyright holder for this preprint (which was not certified by peer review) is the author/funder, who has granted bioRxiv a license to display the preprint in perpetuity. It is made available under aCC-BY 4.0 International license.

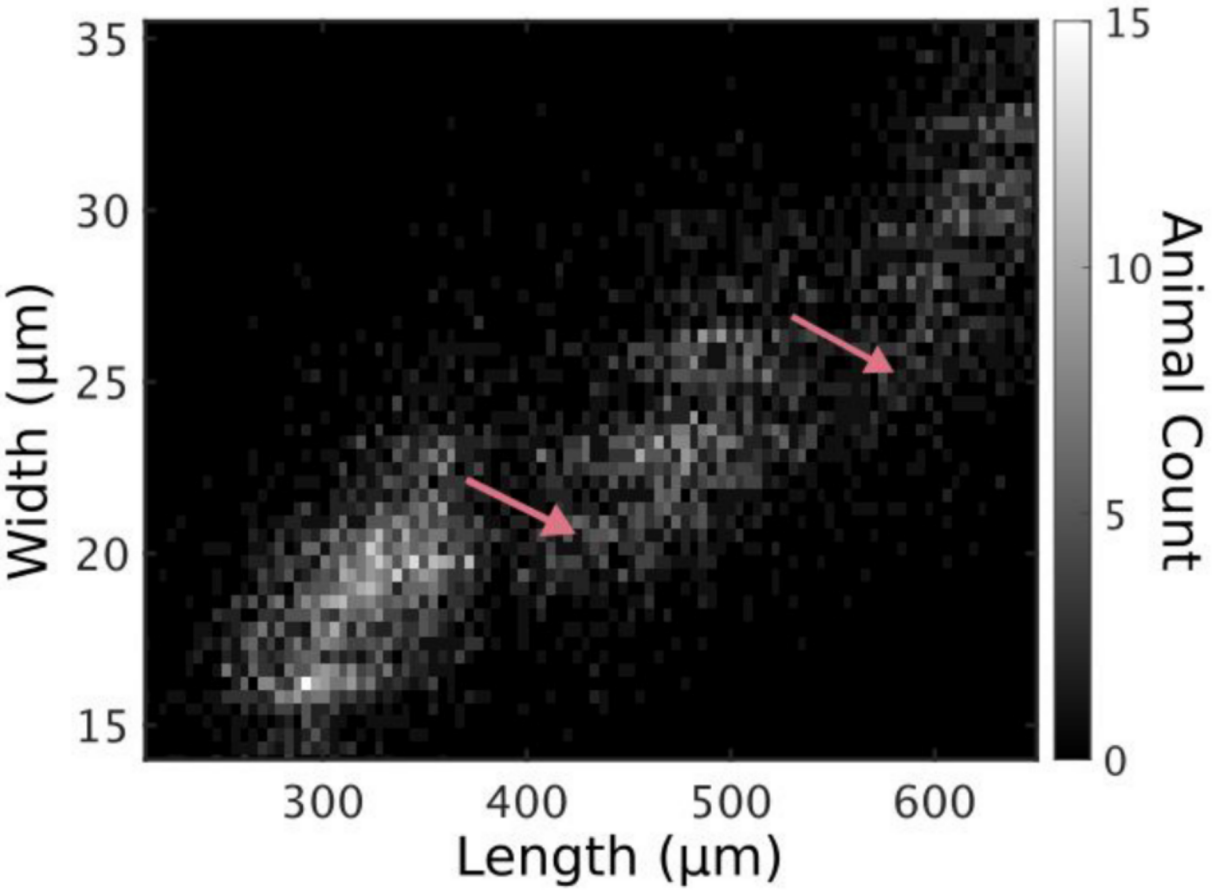

S8 Fig. Animals in all replicates, measured from images

Animal length and width over C. elegans development captured from image data. Higher noise levels in these measurements preclude accurate regressions to individual larval stages. Length jumps and width dips are still apparent. Compare with Fig 6.

bioRxiv preprint doi: https://doi.org/10.1101/2021.04.01.438121; this version posted April 2, 2021. The copyright holder for this preprint (which was not certified by peer review) is the author/funder, who has granted bioRxiv a license to display the preprint in perpetuity. It is made available under aCC-BY 4.0 International license.

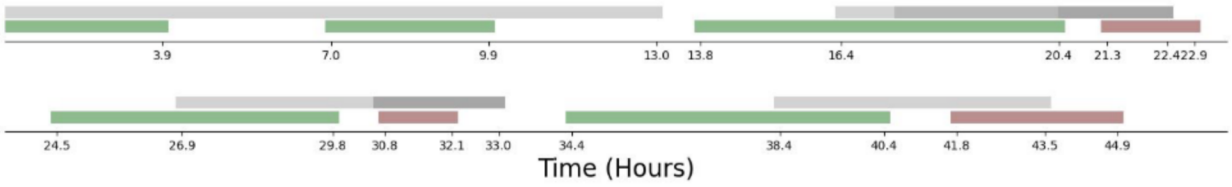

S10 Fig. Timeline of Food Utilization and Stretcher events

In the first row (grey and white) we mark the slopes determined in the Stretcher model. Transition from lighter to darker grey indicates a step increase in slope corresponding to a stiffening cuticle in the length direction. White regions denote time between larval stages. L2 and L3 are the only stages at which we have useful slope information due to the dauer decision in L1 making transitions difficult to determine and the high level of population desynchronization in L4. In the second row (green, red, and white) we mark the food and growth correlations found in (Fig 5B). Green corresponds to times at which both growth rate and food rate are increasing. Red corresponds to times at which both growth rate and food rate are decreasing. White corresponds to times at which growth rate and food rate are uncorrelated. Transitions from green to red regions occur at roughly the same times as the transition to a stiffer cuticle in the length direction.

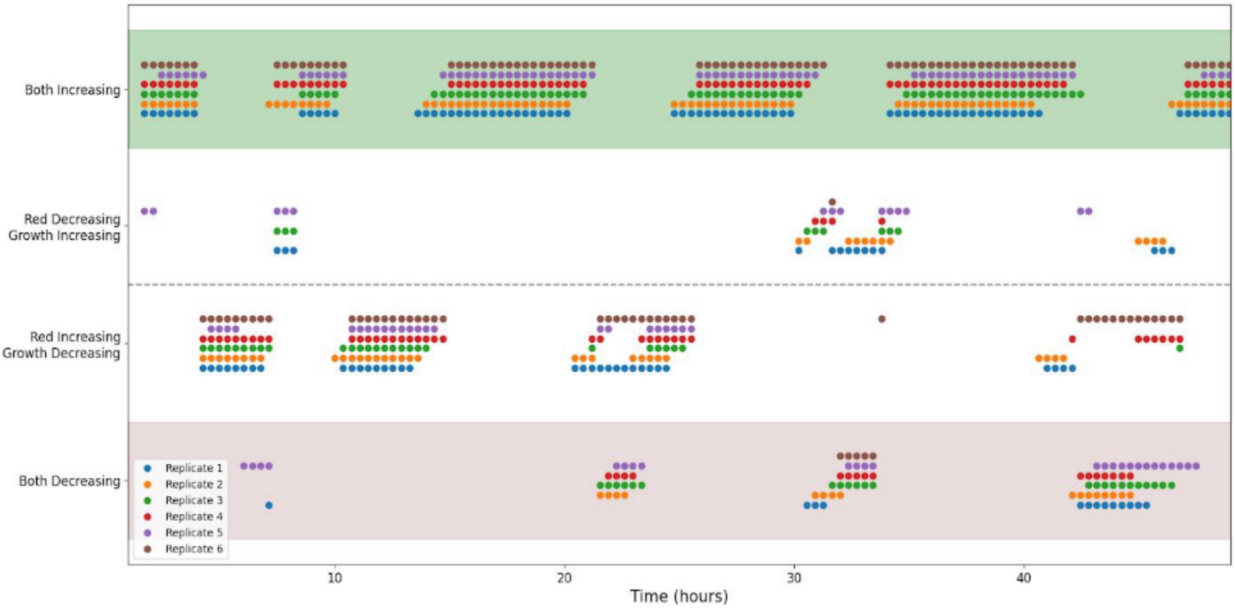

S11 Fig. Analysis of Food intake and growth rate correlation for all replicates

Summary of analysis in Fig 8 for all replicates. Until larval stage L4, most replicates follow the same pattern of transitions from one growth regime to the next. The time delay at transitions in later replicates can be explained by the temperature gradient and differences in growth between replicates.

bioRxiv preprint doi: https://doi.org/10.1101/2021.04.01.438121; this version posted April 2, 2021. The copyright holder for this preprint (which was not certified by peer review) is the author/funder, who has granted bioRxiv a license to display the preprint in perpetuity. It is made available under aCC-BY 4.0 International license.

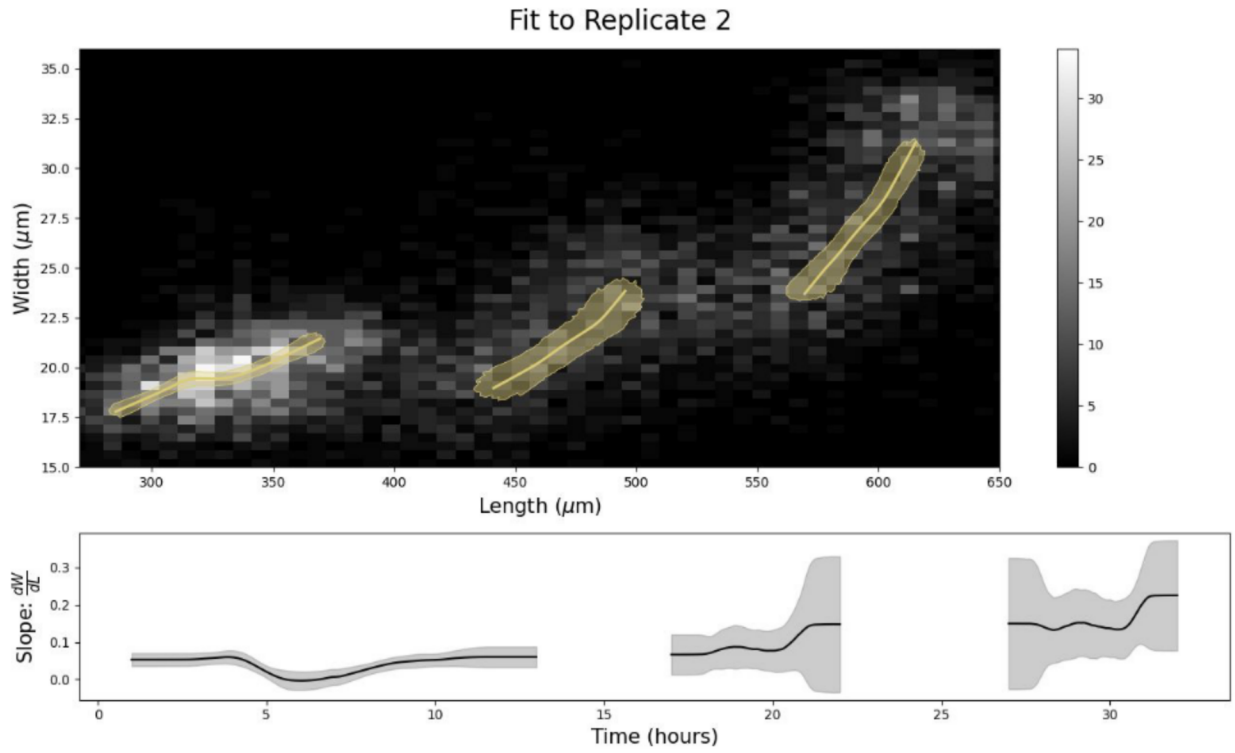

S12 Fig. Stretcher model analysis of replicate 2 COPAS BIOSORT data for different stage thresholding

Compare to Fig 5. Larval hours defined by taking the ceiling of the lower boundary and the floor of the upper boundary. This rounding method for larval stage definition demonstrates the sensitivity of the analysis to edge effects. The unexpected step in the L2 larval stage (Fig 5) is significantly reduced with this rounding method.

bioRxiv preprint doi: https://doi.org/10.1101/2021.04.01.438121; this version posted April 2, 2021. The copyright holder for this preprint (which was not certified by peer review) is the author/funder, who has granted bioRxiv a license to display the preprint in perpetuity. It is made available under aCC-BY 4.0 International license.

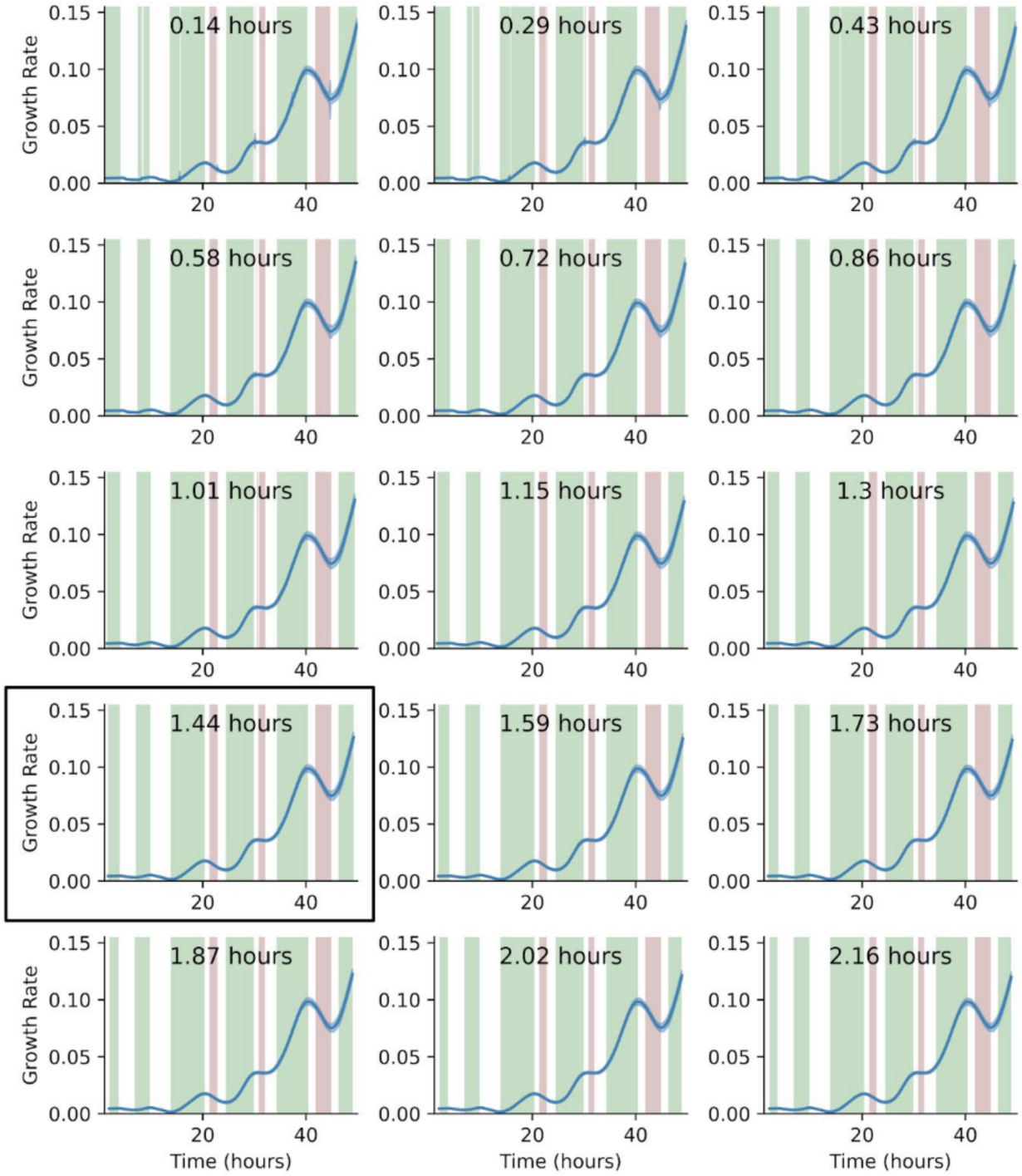

S13 Fig. Sensitivity analysis to moving average window size.
Varying lengths of window sizes (0.14 to 2.16 hours) were calculated for the *lokern* growth rate regression. Window size was increased until the growth rate regression was smoothed. A window size of 1.44 hours (or 0.72 hours on either side of each time point) was chosen to calculate the start and end times of each regime (Fig 8). Continued increase of window size past 1.44 hours did not change the pattern of regimes or their boundaries significantly.

bioRxiv preprint doi: https://doi.org/10.1101/2021.04.01.438121; this version posted April 2, 2021. The copyright holder for this preprint (which was not certified by peer review) is the author/funder, who has granted bioRxiv a license to display the preprint in perpetuity. It is made available under aCC-BY 4.0 International license.

Model Derivations

Bootstrapping Algorithm

To calculate a robust regression of the measured COPAS BIOSORT data we bootstrap the regression using case-resampling (Davison and Hinkley 1997, pages 261-266). Each iteration of the algorithm (**Algorithm S1**) involves resampling the data of interest with replacement and maintaining the size of the sample. At each iteration the lokern regression is calculated for Red, Length, and Width data. Additionally any desired function (for example, volume, pumping frequency times pharynx fraction, or derivatives) of these regressions is calculated at each iteration. Regressions at each iteration are saved and the mean and variance of these regressions at each regression time point are used to determine the statistics of the regression.

Algorithm S1 Regression Bootstrapping with Case Resampling

Ndata = # animals in sample;
iterations = # resamplings;

for $i = 0$ to iterations **do**
  Resample Ndata points with replacement. Collect Red, Length, Width data;

  Apply lokern regression to resampled Red, Length, Width;

  Calculate desired functions of Red, Length, Width regressions;

  Save Red, Length, Width, and combined regressions;
end for

Calculate Standard deviation at each regression time point of saved regressions;

Derivation of eating model

We begin by defining the instantaneous rate of food intake as a function of the flow rate of media through the buccal cavity and the cross sectional area of the buccal cavity.

$$\frac{dV_{food}}{dt} = A_{buccal} \tag{S1}$$

We then make the assumption that the uptake of media fills the pharynx cavity we have

$$\frac{dV_{food}}{dt} = C\frac{dV_{pharynx}}{dt} \tag{S2}$$

We average both sides of the equation under the assumption that the pumping period is significantly shorter than the time scale of growth

bioRxiv preprint doi: https://doi.org/10.1101/2021.04.01.438121; this version posted April 2, 2021. The copyright holder for this preprint (which was not certified by peer review) is the author/funder, who has granted bioRxiv a license to display the preprint in perpetuity. It is made available under aCC-BY 4.0 International license.

$$\frac{1}{T}\int_0^T \frac{dV_{food}}{dt}dt = \frac{1}{T}\int_0^T CA_{buccal} \tag{S3}$$

The integral on the right hand side is the total food intake during a single pumping period.

$$\frac{1}{T}\int_0^T \frac{dV_{food}}{dt}dt = \frac{1}{T}\Delta V_{food} \tag{S4}$$

We then take into account that food is not transported to the gut in the same step as its uptake. Thus the total food intake during a single pump can be calculated by the amount of food that fills the fully opened pharynx

$$\frac{1}{T}\int_0^T \frac{dV_{food}}{dt}dt = \frac{C}{T}V_{pharynx:max} \tag{S5}$$

We then replace the average on the right hand side with the average food intake rate over the pumping period. For simplicity and because we will deal entirely with the average food intake rate, we do not use a different notation for this average rate.

$$\frac{dV_{food}}{dt} = \frac{C}{T}V_{pharynx:max} = Cf(t)V_{pharynx:max} \tag{S6}$$

0.1 Transformation of sorter measurements to volume units

To utilize sorter measurements and convert them to meaningful units we define a linear transformation from the correlation plots (S1 Fig)

$$L = a_1 TOF + b_1 \tag{S7}$$

$$W = a_2 norm.EXT + b_2. \tag{S8}$$

Using Equations (S7) and (S8) we can approximate the volume of any object that passes through the sorter by the expression

$$V = \frac{\pi}{4}(a_1 TOF + b_1)(a_2 norm.EXT + b_2)^2. \tag{S9}$$

bioRxiv preprint doi: https://doi.org/10.1101/2021.04.01.438121; this version posted April 2, 2021. The copyright holder for this preprint (which was not certified by peer review) is the author/funder, who has granted bioRxiv a license to display the preprint in perpetuity. It is made available under aCC-BY 4.0 International license.

Defecation analysis

We use the defecation results found in (Liu and Thomas 1994) to determine if red fluorescent measurements can be used as a proxy for food intake rate as opposed to the instantaneous food volume in the gut. Defecation in adults happens very regularly, with a period of $T_d = 45 \pm 3s$, with $h_d = 43 \pm 10\%$ of their intestinal volume being expelled each time. The volume expelled is well mixed. Defining V_f as the current amount of food in the nematode gut. We can use conservation of mass to state that the rate of change in the amount of food in the gut is equal to the rate of food intake through eating less the defecation rate and the rate at which food volume is metabolized into cell products:

$$\frac{dV_f}{dt} = \left.\frac{dV_f}{dt}\right|_{eating} - \left.\frac{dV_f}{dt}\right|_{defecating} - \left.\frac{dV_f}{dt}\right|_{metabolized} \tag{S10}$$

Using red fluorescence as a proxy for food intake we can ignore the metabolism term as the fluorescent beads are not metabolized.

$$\frac{dV_f}{dt} = \left.\frac{dV_f}{dt}\right|_{eating} - \left.\frac{dV_f}{dt}\right|_{defecating} \tag{S11}$$

Equation (S11) states that the rate of change of the volume of fluorescent beads in the gut is equal to the difference between the intake of red fluorescent beads minus the defecation rate of red fluorescent beads. Using the results of (Liu and Thomas 1994) for the second term, and defining $V_{f:max}$ as the volume of food in the gut just prior to defecation, h_d as the fraction of food expelled during a single defecation cycle, and T_d as the period of defecation. We average Equation (S11) over short time periods to remove the pumping and defecation period oscillations.

$$\frac{dV_{red:max}}{dt} = \left.\frac{dV_red}{dt}\right|_{eating} - \frac{V_{red:max} h_d}{T_d} \tag{S12}$$

On the left hand side, the instantaneous rate of the gut red fluorescence in Equation (S11) is replaced by the rate of change of the maximum or "full" gut fluorescence. The second term on the right hand side of Equation (S11) has been replaced by the average defecation rate over a cycle calculated by multiplying the full gut fluorescence by the fraction expelled and dividing by the defecation period. We solve Equation (S12) for the average eating rate.

$$\left.\frac{dV_{red}}{dt}\right|_{eating} = \frac{dV_{red:max}}{dt} + \frac{V_{red:max} h_d}{T_d} \tag{S13}$$

We take the local regression of the red fluorescence to determine $V_{red:max}(t)$. This value is plugged into

bioRxiv preprint doi: https://doi.org/10.1101/2021.04.01.438121; this version posted April 2, 2021. The copyright holder for this preprint (which was not certified by peer review) is the author/funder, who has granted bioRxiv a license to display the preprint in perpetuity. It is made available under aCC-BY 4.0 International license.

the second term on the right hand side of Equation (S13) and its derivative is used to approximate the first term on the right hand side of Equation (S13). We take the adult values of h_d and T_d (Liu and Thomas 1994) as a first approximation. Figure (S6) demonstrates a comparison of the red fluorescence and the red intake rate with defecation taken into account at the constant adult rates and quantities. We have scaled both the pink curve denoting red fluorescence and the blue curve denoting red intake rate by their maximum. This scaling allows us to see that the two curves are only a multiplicative factor apart up to error bars. This allows us to use the red measurement as a proxy for both red and food intake rates.

Derivation of Stretcher Model

We model the cuticle as a thin walled pressure vessel made of orthotropic, linear materials to capture the relationship between how much the cuticle stretches and the force applied to the cuticle. The relationship between the amount of stretch and the amount of applied pressure is described by the matrix:

$$\begin{bmatrix} \varepsilon_L \\ \varepsilon_{Circ} \end{bmatrix} = \begin{bmatrix} \frac{1}{E_L} & \frac{-v_{cl}}{E_c} \\ \frac{-v_{lc}}{E_L} & \frac{1}{E_c} \end{bmatrix} \begin{bmatrix} \sigma_L \\ \sigma_{Circ} \end{bmatrix} \tag{S14}$$

Here E_L and E_C are the Young's modulus in the length and circumferential direction, and v_{cl} and v_{lc} are the appropriate Poisson's ratios. These material properties can be measured experimentally. Normalized stretch, ε, is defined as the change in size normalized by the initial size of a cuticle in length (L) and circumference (Circ) (**Equations S15 - S16**) . Here σ is the normalized force applied along the length and circumferential directions of the cuticle (**Equations S18 - S19**).

$$\varepsilon_L = \frac{\Delta L}{L_0} \tag{S15}$$

$$\varepsilon_{Circ} = \frac{\Delta Circ}{Circ_0} \tag{S16}$$

Here L_0 and $Circ_0$ are the length and circumference of the cuticle at the onset of stretch, or in other words at the start of a larval stage. Experimentally we measure width, not circumference, but the circumference of a circle is proportional to the width of the circle, so we can replace the circumference with the measured width:

$$\frac{\Delta Circ}{Circ_0} = \frac{\pi \Delta W}{\pi W_0} = \frac{\Delta W}{W_0} \tag{S17}$$

By approximating *C. elegans* as cylindrical, and assuming the only force working on the cuticle is isotropic

bioRxiv preprint doi: https://doi.org/10.1101/2021.04.01.438121; this version posted April 2, 2021. The copyright holder for this preprint (which was not certified by peer review) is the author/funder, who has granted bioRxiv a license to display the preprint in perpetuity. It is made available under aCC-BY 4.0 International license.

internal pressure, we can determine the normalized force in terms of pressure and geometric properties:

$$\sigma_L = \frac{r}{2t}\Delta p \tag{S18}$$

$$\sigma_{Circ} = \frac{r}{t}\Delta p \tag{S19}$$

Where r is the radius of the cylinder and t is the thickness of the cuticle. We can now rewrite Equation (S14) in terms of measurable quantities (length and width) by multiplying out the matrices making the appropriate substitutions.

$$\Delta L = \frac{L_0 r}{t}\left(\frac{1}{2E_L} - \frac{v_{cl}}{E_c}\right)\Delta p = a_L \Delta p \tag{S20}$$

$$\Delta W = \frac{W_0 r}{t}\left(\frac{1}{E_C} - \frac{v_{lc}}{E_L}\right)\Delta p = a_W \Delta p \tag{S21}$$

Here we compress the coefficients fixed by material and geometric properties into one constant

$$a_L = \frac{L_0 r}{t}\left(\frac{1}{2E_L} - \frac{v_{cl}}{E_c}\right) \tag{S22}$$

$$a_W = \frac{W_0 r}{t}\left(\frac{1}{E_c} - \frac{v_{lc}}{E_L}\right) \tag{S23}$$

Stretcher Slope Calculations

The Stretcher model predicts a constant ratio between stretch in width, ΔW, and stretch in length, ΔL. These measures of stretch are changes in the length and width measurements over some period of time. To see how the ratio of $\frac{\Delta W}{\Delta L}$ changes throughout a larval stage, we need to measure the stretch instantaneously. To do this we take advantage of the derivative approximation

$$\Delta W \approx \frac{dW}{dt}\Delta t \tag{S24}$$

$$\Delta L \approx \frac{dL}{dt}\Delta t \tag{S25}$$

Equations (S24, S25) are combined in the ratio found in Equation (3) to give:

$$\frac{\Delta W}{\Delta L} \approx \frac{W'(t)}{L'(t)} \tag{S26}$$

bioRxiv preprint doi: https://doi.org/10.1101/2021.04.01.438121; this version posted April 2, 2021. The copyright holder for this preprint (which was not certified by peer review) is the author/funder, who has granted bioRxiv a license to display the preprint in perpetuity. It is made available under aCC-BY 4.0 International license.

Here $W' = \frac{dW}{dt}$ and $L' = \frac{dL}{dt}$. We differentiate the time series from the local regressions of length and width data. The ratio of derivatives gives the instantaneous stretch ratio as it changes over time. Due to the numerical difficulty of calculating both derivatives and ratios with accuracy, we expect large error bars for this ratio. To estimate the size of error bars we apply a first order error propagation formula to Equation (S26).

$$\sigma^2_{Ratio} \approx \left|\frac{\partial Ratio}{\partial(W')}\right|^2 \sigma^2_{(W')} + \left|\frac{\partial Ratio}{\partial(L')}\right|^2 \sigma^2_{(L')} + 2\frac{\partial Ratio}{\partial(W')}\frac{\partial Ratio}{\partial(L')}\sigma_{(W')(L')} \tag{S27}$$

$$\sigma^2_{Ratio} \approx \left|\frac{1}{L'}\right|^2 \sigma^2_{(W')} + \left|\frac{-(W')^2}{(L')^3}\right|^2 \sigma^2_{(L')} - 2\frac{W'}{(L')^3}\sigma_{(W')(L')} \tag{S28}$$

The variance in Equation (S28) is calculated for each time point in the regressions of length and width. We resample the data for each larval stage 2,000 times with replacement (see Methods for larval stage determination). For each of these resampled sets of data, we numerically differentiate the length and width regression to determine an estimate of the length and width derivatives over time. At each time point the mean regression length and width derivatives are used in place of W' and L'. The covariance matrix for the length and width derivatives is calculated at each time point using the 2,000 resampled regressions in the bootstrap analysis and used as the variance terms in Equation (S28).